



Boosting RNA nanotherapeutics with V-ATPase activating non-inflammatory lipid nanoparticles to treat chronic lung injury

Received: 24 November 2024

Accepted: 30 June 2025

Published online: 14 July 2025

Check for updates

Zhiqiang Zhao^{1,2,3,15}, Xinzhu Shan^{1,2,15}, Jing Ding , Bin Ma^{1,2,15}, Buyao Li^{1,2}, Wendi Huang⁵, Qingqing Yang^{6,7,8,9}, Yian Fang^{1,2}, Junhe Chen¹⁰, Chenglin Song¹, Chenlong Wei^{1,2}, Shuai Liu¹¹, Xingdi Cheng^{11,12}, Shengran Zhang^{1,2}, Yunxuan Liu^{1,2}, Hongkun Wu ¹³, Cong Luo ³, Shaokun Shu ^{6,7,8,9}, Xue Qiao ¹, Zefeng Wang ^{5,14} , Xueguang Lu ^{11,12} & Lei Miao ^{1,2,9}

Lipid nanoparticles (LNPs) are a promising platform for mRNA delivery. However, their use in inflammatory pulmonary diseases is limited by reactogenicity and suboptimal delivery. Here we develop a non-inflammatory LNP (NIF-LNP) by incorporating ursolic acid, identified from a natural product library, into a biodegradable, cationic phosphoramido-derived LNP formulation. NIF-LNPs exhibit a 40-fold enhancement in lung protein expression without causing significant reactogenicity compared to LNPs containing ALC-0315. Our CRISPR-KO mechanistic studies uncover that ursolic acid promote endosome acidification by activating the V-ATPase complex, acting as a central hub for endosomal trafficking of LNPs and inflammation control. Furthermore, we identify an intracellular circadian regulatory gene, NR1D1, encapsulated in NIF-LNPs, showing notable therapeutic efficacy in bronchopulmonary dysplasia and lung fibrosis. To enhance clinical feasibility, we have developed a lyophilized formulation that maintains stability for over 90 days and ensures efficient nebulization in preclinical male mouse, pup rat, and male dog models. Overall, this V-ATPase-activating atomized NIF-LNP presents a viable strategy for treating variable chronic inflammatory lung diseases.

mRNA-based therapeutics have revolutionized the treatment of a spectrum of diseases, ranging from genetic disorders to infectious diseases and malignancies^{1–4}. Lipid nanoparticles (LNPs), proven by their role in mRNA vaccine development against COVID-19, are the only clinically approved mRNA carriers⁵, and have shown remarkable potential in protein replacement therapy and gene editing^{6,7}. However, the clinical application of lipid-formulated RNA vaccines is associated with dose-limiting systemic inflammatory responses in humans, causing many side effects involves pain, swelling, and fever⁸. In contrast to vaccines that elicit a robust immune response with minimal antigen, therapeutic mRNA requires up to 1000 times more protein to meet the

therapeutic window^{9–11}. This heightened requirement can lead to increased reactogenicity, an immune response characterized by inflammation and side effects, and may conversely decrease mRNA transfection efficiency by activating endogenous RNA sensor¹². The inherent reactogenicity of LNPs can exacerbate the progression of many chronic diseases that are often associated with inflammation, thereby introducing additional challenges to the use of mRNA therapeutics for treating chronic diseases^{13–15}. Both we and others have found that the reactogenicity is significantly heightened in animal models with chronic diseases background, sometimes even leading to mortality^{16,17}. Consequently, the key missing link to unlocking mRNA's

A full list of affiliations appears at the end of the paper. e-mail: dingjingvv@126.com; wangzf@sustech.edu.cn; xueguang@iccas.ac.cn; lmiao_pharm@bjmu.edu.cn

full potential as therapeutics is to improve mRNA delivery efficiency while minimizing reactogenicity.

The immunogenicity of mRNA-loaded LNP arises from mRNA and the lipid components¹⁸. Modifications like N1-methyl-pseudouridine can help reduce the immune response triggered by mRNA, but the ionizable cationic lipids required for mRNA encapsulation and release from endosomes also provoke reactogenicity^{10,19,20}. As these lipids facilitate endosome escape, they can also damage endosomal membranes, leading to mRNA release and inadvertently initiating an inflammatory response that attracts leukocytes and results in immune reactions^{18,21}. Previous efforts to tackle these issues included adding anti-inflammatory agents and creating less immunogenic lipids^{22–26}. However, achieving a marked increase in protein expression while minimizing endosomal damage has proven to be a persistent challenge.

In the context of pulmonary therapy, the lung has a high susceptibility to infection and inflammation due to its constant exposure to external air, necessitating a cautious approach to mRNA LNP safety²⁷. The two primary routes of lung administration—systemic intravenous injection and local inhalation—each present unique challenges^{6,16,28}. Systemic administration often involves high cationic lipid content, thus leading to elevated toxicity⁶. Local inhalation, though avoiding systemic toxicity, can result in acute lung inflammation and even fatal outcomes with excessive LNP accumulation^{16,28}. Current pulmonary delivery of mRNA has predominantly focused on the development of efficient carriers to enhance mRNA expression and nebulization stability^{29–31}. However, these efforts have not adequately addressed the intrinsic toxicity and immunogenicity of LNPs, which may restrict their clinical utility.

Here, we show an effective non-inflammatory LNP (NIF-LNP) designed for superior protein expression in the lung with significantly minimized reactogenicity. Our approach involves the creation of a phosphoramido-derived ionizable cationic lipid library, which enables the discovery of a lipid with 6-fold higher delivery efficiency than the commercial ALC-0315 formulation. Building on this, we identify ursolic acid from 22 natural products, which further promotes mRNA expression as a fifth component of the NIF-LNP, with over 40-fold enhancement compared to ALC-0315 without causing inflammation. Specifically, leveraging genome-wide CRISPR screen, we pinpoint vacuolar-type ATPase (V-ATPase) as a critical regulator in resolving the expression/reactogenicity dilemma. As a key modulator for endosomal function, V-ATPase interacts with ursolic acid to improve mRNA expression without causing additional immunogenicity. We further demonstrate the therapeutic potential of NIF-LNPs in the models of neonatal bronchopulmonary dysplasia (BPD) and adult idiopathic pulmonary fibrosis (IPF) by delivery of an mRNA encoding the nuclear receptor subfamily 1 group D member 1 (NR1D1), a target inaccessible via direct protein therapy. We also optimize the storage and nebulization stability of NIF-LNP to facilitate clinical application. This work not only establishes a promising V-ATPase-engaged mRNA LNP-based therapeutic strategy for pulmonary inflammatory diseases but also provides a rationale for harmonizing efficacy and reactogenicity in mRNA therapeutics, paving the way for safer and more effective mRNA-based treatments.

Results

Construction of phosphoramido lipid (PL) library for RNA delivery to lung and their inflammation evaluation

The low degradation rate and prolonged tissue accumulation of ionizable cationic lipids are key issues that lead to excessive innate immune activation by LNPs³². In our previous study, we identified PL14, an ionizable cationic lipids with a piperazine-centered phosphoramido core structure (PL), exhibiting more than 60-fold higher transfection efficiency in the joint cavity after local administration compared to the commercialized MC3 LNP formulations³³. To enhance the in vivo

degradation and clearance of PL14 lipid, we constructed and purified a group of biodegradable PLs by introducing various ester and amide bonds into its head and tails for in-situ lung mRNA delivery (Fig. 1a–c and Figure S1). To identify lead candidates, LNPs comprising ionizable PLs, together with other helper lipids (including 1,2-distearoyl-sn-glycero-3-phosphorylcholine (DSPC), cholesterol and 1,2-dimyristoyl-rac-glycero-3-methoxypolyethylene glycol-2000 (DMG-PEG₂₀₀₀)), were prepared following a classical formulation ratio (PLs: DSPC: Cholesterol: DMG-PEG₂₀₀₀ = 50: 10: 38.5: 1.5) and loaded with firefly luciferase mRNA (mLuc) (Fig. 1d). The encapsulation efficiency of LNPs with ionizable PLs (PL LNPs) was between 65% and 80% (Figure S2). At 6 h after intratracheal administration, the transfection potency was measured via the luminescence signal in the lung using IVIS imaging (Fig. 1e, f and Figure S3a). In the first round of screening, we found that introducing degradable linkers adjacent to the piperazine core (PL24 and PL26) reduced the delivery efficiency of mLuc as compared to PL14. With the core structure fixed, we identified that adding ester linkage at the distal end of the phosphoramido linker would compromise mLuc delivery efficiency, whereas adding branched ester tails next to the phosphoramido bond significantly improved mLuc expression in the lung. Finally, we identified a top candidate lipid, PL32 (R_{2a}-Head₁-R_{1b}, Fig. 1b and c), which displayed the highest protein expression efficiency, with nearly a 14-fold, 6-fold, and 2-fold increase compared with LNPs formulated with MC3, ALC-0315, and cKK-E12 respectively (Fig. 1e, f and Figure S3a).

To investigate the immunogenicity of the PL lipids, we collected the bronchoalveolar lavage (BAL) fluid 24 h after mLuc LNP treatment and analyzed the cytokine levels (Fig. 1g). To mitigate the inherent immunogenicity of mRNA, 100% N1-methyl-pseudouridine-modified mRNAs were utilized in our study¹⁷. We observed a significant increase in the levels of IL-1 β , IL-6, and TNF- α following administration of mLuc LNPs, compared to blank mice (Figure S3b). Furthermore, a strong positive log-linear correlation was identified between cytokine secretion and the efficiency of mLuc delivery by the LNPs (Fig. 1h, i). We also evaluated the inflammatory response of empty PL LNPs and other reported LNPs formulation without mRNA such as those with MC3, ALC-0315, and cKK-E12 by incubating with pro-inflammatory macrophages. The previously noted pro-inflammatory cytokines induced by LNPs were measured by qPCR^{11,12,24,34,35}. Consistently, these LNPs caused a significant upregulation of inflammatory genes suggesting the generation of inflammation (Figure S3c). This finding indicated that the ionizable cationic lipid vehicles are the main drivers of the observed reactogenicity. Notably, the lead LNP, PL32 (Fig. 1j), exhibited the highest mRNA in vivo delivery efficiency and a favorable inflammation-to-expression ratio among the tested LNPs (Fig. 1e–h).

Gene replacement therapy often requires high-dose repetitive administration to achieve satisfactory therapeutic protein levels⁹. However, such treatments can exacerbate lung damage in conditions characterized by inflammation¹⁶. To investigate this, we delivered a single high-dose of mLuc (0.6 and 1.2 mg/kg) using MC3, ALC-0315, or PL32 formulations, directly into the lungs of mice with LPS-induced acute lung injury (ALI) or the bleomycin-induced idiopathic pulmonary fibrosis (IPF) models via intratracheal instillation. BAL samples collected at 24 h post-administration showed a 2–6-fold increase in cytokine levels in ALI and IPF mice when compared to healthy controls (Figure S3d and e), confirming the establishment of the models. This increase in cytokine secretion was further exacerbated following the high-dose LNP treatment, showing a 4–28-fold escalation and in a dose-dependent manner (Figure S3d and e). Gross anatomical inspection of the lungs from ALI mice administrated with 0.6 mg/kg of mLuc in LNPs revealed severe “hepatization”, a clear sign of lung inflammation (Fig. 1k)²¹. Further lung histological analysis confirmed increased immune cell infiltration, alveolar rupture, and thickening of alveolar septa after LNP administration (Fig. 1k). More importantly, the repeated dosing of LNPs encapsulated GMP grade mLuc to IPF mice at

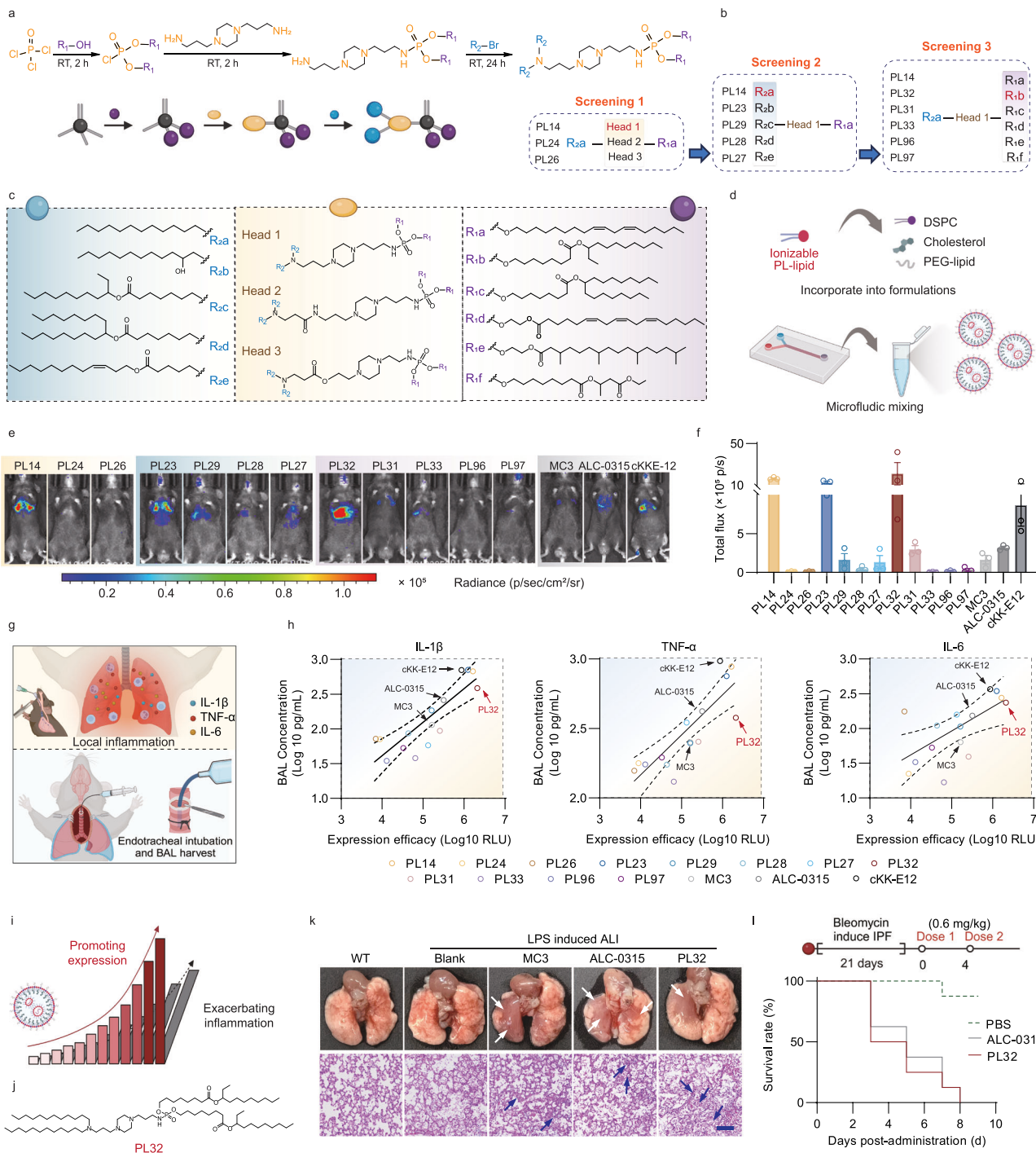


Fig. 1 | Development of phosphoramide lipid (PL) library for lung targeting RNA delivery and their inflammation evaluation. **a** Schematic of phosphorus oxychloride-mediated multicomponent reactions (PMR) in the synthesis of PLs. RT: Room temperature. **b, c** Structures of the three components of PLs used in the synthesis library and the screening process. **d** Preparation of PL LNPs by a microfluidic device. **e** Expression of mLuc at 6 h after intratracheal administration of the PL LNPs, the original MC3, ALC-0315, or cKK-E12 LNPs (0.2 mg/kg, $n = 3$ mice, one representative mouse in each group were shown). **f** Quantification of (e). **g** Schematic illustration of lipid nanoparticle (LNP) induced lung inflammation and collection of bronchoalveolar lavage (BAL). **h** Correlation analysis between cytokine secretion and mLuc expression after intratracheal administration of the PL LNPs. Measurement of IL-1 β , IL-6, and TNF- α concentration were conducted using ELISA assay in BAL collected at 24 h after intratracheal administration of the PL LNPs ($n = 3$ mice in each group, mean values were presented).

i Schematic shows the positive correlation of cytokine concentration and luciferase expression. **j** Chemical structure of PL32. **k** Gross anatomical images and H&E staining of lungs from healthy mice and ALI mice intratracheally instilled with PBS or single dose 0.6 mg/kg of mLuc in MC3 LNP, ALC-0315 LNP, and PL32 LNP. $n = 3$ mice per group with similar results. Scale bar, 100 μm . Arrows indicate the areas of hepatization and inflammation. **l** Survival curve of bleomycin induced pulmonary fibrosis mice after two doses of mLuc LNP treatment (0.6 mg/kg, $n = 8$ mice in each group). Data were represented as mean \pm SEM. Figure (a, c, d, g, i, l) were created in BioRender.com with attribution line Miao, L. (2025) <https://BioRender.com/p99f207>, Miao, L. (2025) <https://BioRender.com/a31ebmk>, Miao, L. (2025) <https://BioRender.com/g9lq68b>, Miao, L. (2025) <https://BioRender.com/kfsouj6>, Miao, L. (2025) <https://BioRender.com/v99qge> and Miao, L. (2025) <https://BioRender.com/qrqgh2s>, respectively. Source data are provided as a Source Data file.

0.6 mg/kg led to a 100% mortality rate (Fig. 1i). This suggests that the severe reactogenicity caused by ionizable cationic LNPs can be detrimental to patients with chronic lung inflammation, posing an enormous hurdle for RNA nanotherapeutics in treating lung-related injuries.

Incorporation of natural products in LNPs promoted mRNA expression and relieve inflammation

To relieve reactogenicity, promote mRNA expression, and break their positive correlation (Fig. 1i), we explored the integration of hydrophobic natural anti-inflammatory products with minimal reported toxicity profiles^{36,37}. Through a literature-informed selection, we introduced 22 natural-anti-inflammatory products (NAIPs) as an additional component in our LNP formulations, including four main subclasses: (I) tetracyclic triterpenoids, (II) flavonoids, (III) pentacyclic triterpenoids, and (IV) other phenols (Fig. 2a and Figure S4a). These NAIPs were incorporated at a 20% mol ratio of the total lipid content, complementing our proprietary ionizable cationic lipid, PL32, without RNA loading. Of these, 17 NAIPs were successfully encapsulated within LNPs, forming stable NAIP LNPs that were then utilized for subsequent experiments (Figure S4b).

We proceeded to evaluate the capacity of NAIPs to mitigate the inflammatory response elicited by LNPs (without mRNA) in pro-inflammatory macrophages. Both PL32 LNPs and NAIP LNPs were applied to pro-inflammatory macrophages, activated with LPS and IFN- γ for a duration of 24 h (Figure S5a). Consistent with the results depicted in Figure S3c, PL32 LNPs induced a substantial upregulation of inflammatory cytokines including *Il-1 β* , *Il-6*, *Tnf- α* , and *Ccl5*, with increases ranging from 10- to 57-fold (Figure S5a). In contrast, the incorporation of NAIPs into LNPs markedly mitigated these inflammatory responses. Notably, the addition of calycosin, ursolic acid, protopanaxatriol, and phillygenin to the LNPs resulted in a 3-10-fold decrease in *Il-1 β* and *Il-6* levels compared to PL32 LNPs, approaching levels comparable to the wild-type (WT) M1-type macrophages (Figure S5a). These effects were similar to, or in some cases, exceeding the anti-inflammatory effects of dexamethasone (Dex) when added to LNPs at equivalent doses (Figure S5a).

We next evaluated the transfection efficiency of mLuc-encapsulated NAIP LNPs in A549 lung epithelial cells. NAIPs were included at concentrations ranging from 10 mol% to 30 mol% of the total lipid component (Table S1). The photos and physicochemical properties of representative NAIP LNPs with 20 mol% adding were exhibited in Figure S4b and Table S2, respectively. Most of these NAIP LNPs, except those with Rheinic acid, exhibited a similar particle size within 100–200 nm and encapsulation efficiency (EE) between 65%–80%. Additionally, the incorporation of acidic-derived NAIPs resulted in reduced surface charge, which is likely attributed to the rearrangement of the carboxyl-polar head groups on the surface due to electrostatic repulsion during the dialysis process³⁰. For the protein expression, we discovered that incorporating most flavonoids and pentacyclic triterpenoids in PL32 LNPs significantly boosted mLuc expression (Fig. 2b and Figure S6). Specifically, the addition of 10% calycosin (CAL), 20% asiatic acid (AA), 20% ursolic acid (UA), and 20% oleanolic acid (OA) led to expression increases of 6.2-, 8.7-, 14.3-, and 12.8-fold compared to the original PL32 LNPs, respectively (Fig. 2b). Such trend was diminished when adding 30% of AA, UA, and OA (Figure S6). In contrast, LNPs containing Dex showed a decrease in mLuc expression across all the tested ranges (Fig. 2b and Figure S6). Intriguingly, the lead NAIPs (AA, UA, OA) showing the highest mLuc expression with minimal inflammation shared a common structural feature: the presence of a C-3 hydroxyl group and a C-28 carboxyl group (Fig. 2c). Esterification of the 3-hydroxyl group, as seen with OA and its 3-acetate derivative, reduced mLuc expression and increased inflammation (Fig. 2b, c, Figure S5a and S6). Moreover, the removal of the C-28 carboxyl group, when comparing UA with α -Amyrin, was

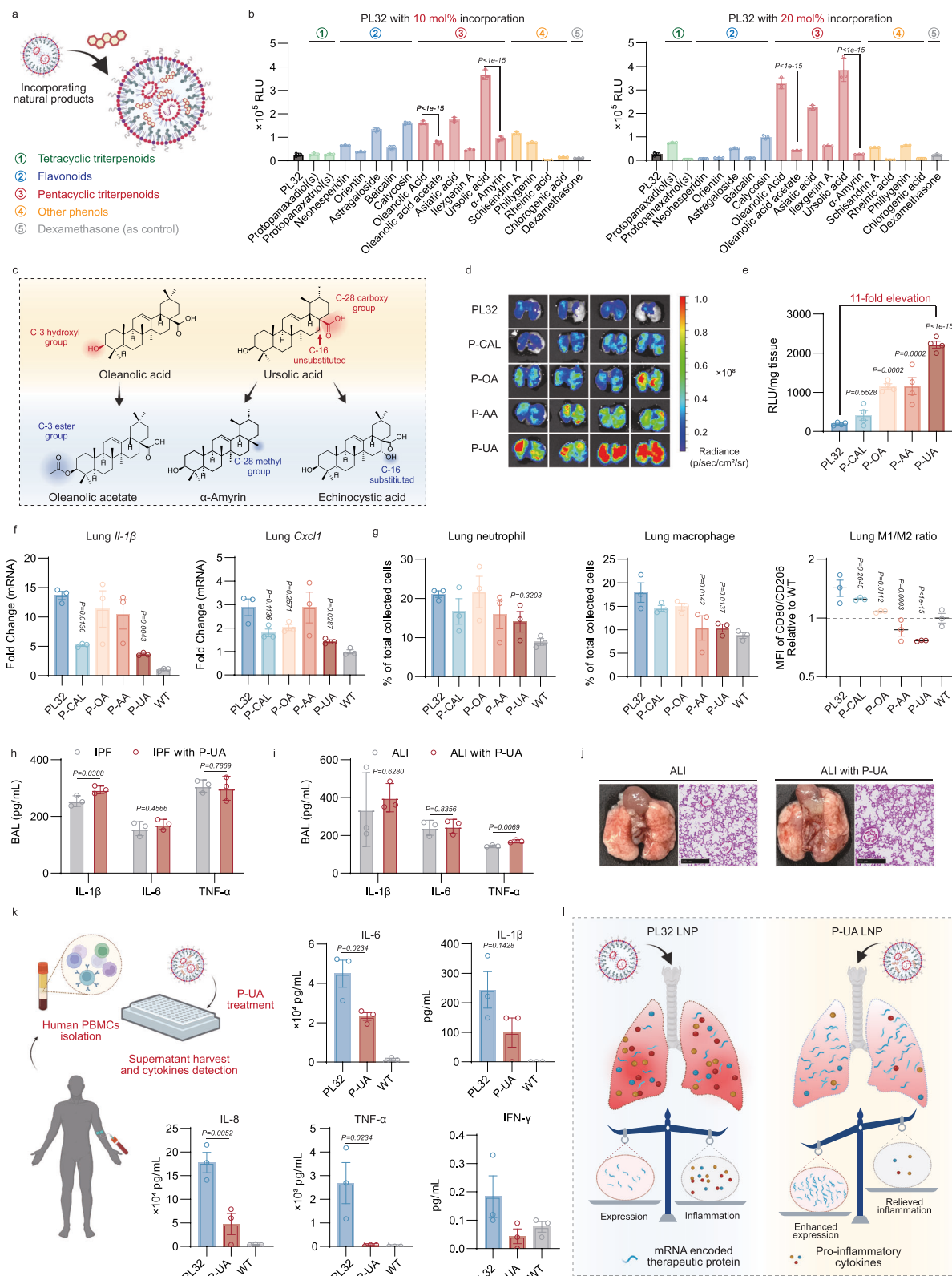
detrimental to mLuc expression and inflammation relief (Fig. 2b, c, Figure S5a and S6). Furthermore, the introduction of hydroxyl groups at the C-16 position was unfavorable for LNP encapsulation, as evidenced by the comparison between UA and echinocystic acid (Fig. 2c and Figure S4b).

We further validated whether adding NAIPs can improve mRNA expression in other cell models or encapsulating mRNA encoding other reporter genes (Figure S5b and c). The lead candidate NAIP LNPs containing 10 mol% CAL, 20 mol% AA, 20 mol% UA, and 20 mol% OA (P-CAL, P-AA, P-UA, and P-OA LNPs) were formulated and compared to control PL32 LNPs. All five formulations had particle sizes of approximately 120 nm, a polydispersity index (PDI) below 0.2, and encapsulation efficiencies exceeding 65% (Table S3). The P-AA, P-UA, and P-OA LNPs showed a higher negative charge due to the presence of carboxyl groups (Table S3). Similar trends were observed in pulmonary microvascular and umbilical endothelial cells, pulmonary and bronchial epithelial cells, as well as immune cells (Figure S5b). P-UA LNPs were also able to enhance the delivery of GFP mRNA (mGFP) with 3-6-fold increase at dose of 0.1-0.4 μ g mGFP in A549 cells, and the mGFP expression is dose-dependent (Figure S5c). Then, we intratracheally instilled these LNPs containing mLuc into healthy mice (0.2 mg/kg) and assessed protein expression in lungs after 2 and 6 h. The P-CAL, P-AA, P-OA, and P-UA LNPs significantly enhanced luciferase expression in the lungs, with respective increases of 2- to 11-fold compared to the original PL32 formulation (Fig. 2d, e and Figure S5d). Notably, the P-UA LNPs exhibited a remarkable 40-fold enhancement in lung protein expression, compared to conventional ALC-0315 LNPs (Figure S7). This observation aligned with the in vitro transfection study conducted in A549 cells, underscoring the significant potential of NAIP LNPs for improving mRNA local delivery efficiency. Furthermore, we collected blood and lung tissues to assess the inflammatory responses. P-UA LNPs demonstrated the most potent anti-inflammatory activity, significantly reducing the gene expression of *Il-6* and *Cxcl2* in the lungs, decreasing the infiltration of neutrophils and macrophages, lowering the M1/M2 macrophage ratio in the lungs, and downregulating IL-6 levels in the serum, compared to PL32 LNPs (Fig. 2f, g, Figure S5e, f and S8). Based on these findings, P-UA LNPs were identified as the optimal formulation.

Next, we compared the impact of encapsulating UA and the conventional Dex into LNP mediated mRNA expression and inflammation in vivo. We found that incorporating Dex into PL32 LNPs negatively affected mRNA transfection in lungs, resulting in a slight but not significant reduction of Luc protein expression (Figure S9a). In contrast, encapsulating UA into PL32 LNP caused an over 10-fold protein expression enhancement (Fig. 2d and e). To assess the anti-inflammatory effect, we detected proinflammatory cytokine levels in BAL at 24 h post LNP treatment. Both P-UA LNPs and P-Dex LNPs showed effective anti-inflammatory activity, significant reducing proinflammatory cytokine levels compared to PL32 LNPs (Figure S9b).

Additionally, we found that adding UA to ALC-0315 and cKK-E12 could also significantly enhance protein expression, achieving a 3–5 fold increase at 24 h compared to the original formulations (Figure S10a). Consistently, UA incorporation effectively mitigated pulmonary inflammatory responses, as evidenced by reduced proinflammatory cytokine levels in BAL, serum and the lungs (Figure S10b–d). Together, these results demonstrate that UA incorporation serves as a universal strategy to enhance both the safety and efficacy of LNPs.

We further explored the impact of high-dose P-UA LNPs at 0.6 mg/kg on ALI and IPF mice. Contrary to our previous observations with PL32 LNPs (Figure S3d and e), P-UA LNP treatment did not lead to significant changes in the level of cytokines (i.e., IL-1 β , IL-6, and TNF- α) in the BAL (Fig. 2h and i). Additionally, gross anatomical examination and H&E staining of the lung tissues revealed no signs of hepatization, increased immune cell infiltration, and alveolar damage



when treated with P-UA LNP (Fig. 2j). These findings indicate that P-UA LNP, even at high doses, do not exacerbate the inflammatory condition in mice with pre-existing lung inflammation. We further evaluated the inflammatory responses induced by PL32 LNP and P-UA LNP in human peripheral blood mononuclear cells (PBMCs) (Fig. 2k). A total of 1×10^5 PBMCs were treated with 1 μ g of mLuc encapsulated in PL32 LNP or P-UA LNP for 24 h. Consistent with

mouse studies, the concentrations of IL-1 β , IL-6, IL-8, and TNF- α significantly increased in the group treated with PL32 LNP. Conversely, the levels of these cytokines in the P-UA LNP treated group were significantly lower than PL32 LNP, suggesting the low inflammatory feature of P-UA LNP can be readily translatable to humans (Fig. 2k and Figure S5g). These results confirmed that UA successfully relieves reactogenicity and amplifies mRNA expression. P-UA LNP as

Fig. 2 | Construction of NIF LNPs with improved mRNA transfection efficiency. **a** Adding NAIPs in PL32 LNPs to prepare non-inflammatory NAIP LNPs. **b** In vitro expression of mLuc delivered by NAIP-LNPs formulations in A549 cells. 24 hours after incubation with mLuc LNPs, the expression was measured using a BioTek plate reader ($n = 3$ biologically independent wells). **c** Chemical structures of the lead candidate NAIPs. **d** Expression of mLuc 6 h after intratracheal administration of the representative NAIP-LNPs and the original PL32 LNPs (0.2 mg/kg, $n = 4$ mice). Lung tissues were lysed, and luminescence was detected using a BioTek plate-reader. The quantification of the mLuc expression was presented on the right in (e), P-CAL: PL32 with calycosin; P-OA: PL32 with oleanolic acid; P-AA: PL32 with asiatic acid; P-U: PL32 with ursolic acid, ($n = 4$ mice). **f** Relative mRNA expression of *Il-1 β* and *Cxcl1* in lung tissues of (d) ($n = 3$ mice). **g** Quantification of neutrophils, macrophages, and M1/M2-macrophages by flow cytometry analysis in previous lung tissues of (d) ($n = 3$ mice). **h, i** Inflammatory cytokines levels of BAL in idiopathic pulmonary

fibrosis (IPF) and acute lung injury (ALI) mice intratracheally instilled with PL32 LNPs and P-U LNPs for 24 h (0.6 mg/kg, $n = 3$ mice per group). **j** Anatomical inspection and H&E stain of lung tissues. Scale bar, 100 μ m. **k** Detection of inflammatory cytokines in human peripheral blood mononuclear cells (PBMCs) treated with PL32 LNPs and P-U LNPs for 24 h by Cytometric Bead Array (CBA) - I Kit ($n = 3$ independent wells). **l** Schematic illustration of mRNA expression and inflammation in lung after administration of non-inflammatory P-U LNPs and traditional PL32 LNPs. Data were represented as mean \pm SEM. Statistical significance was calculated through two-tailed unpaired Student's t-test. **(h, i)** One-way ANOVA with Dunnett test (e–g), and One-way ANOVA with Tukey's test (b, k). Figure 2a, k, l were created in BioRender. com with attribution line Miao, L. (2025) <https://BioRender.com/4tk9uu8>, Miao, L. (2025) <https://BioRender.com/7t6a86q> Miao, L. (2025) and Miao, L. (2025) <https://BioRender.com/9bx34ve>, respectively. Source data are provided as a Source Data file.

NIF LNPs exhibited great potential in the treatment of inflammatory pulmonary diseases (Fig. 2l).

NIF P-U LNPs improve mRNA expression and reduce inflammatory injury by activating V-ATPase

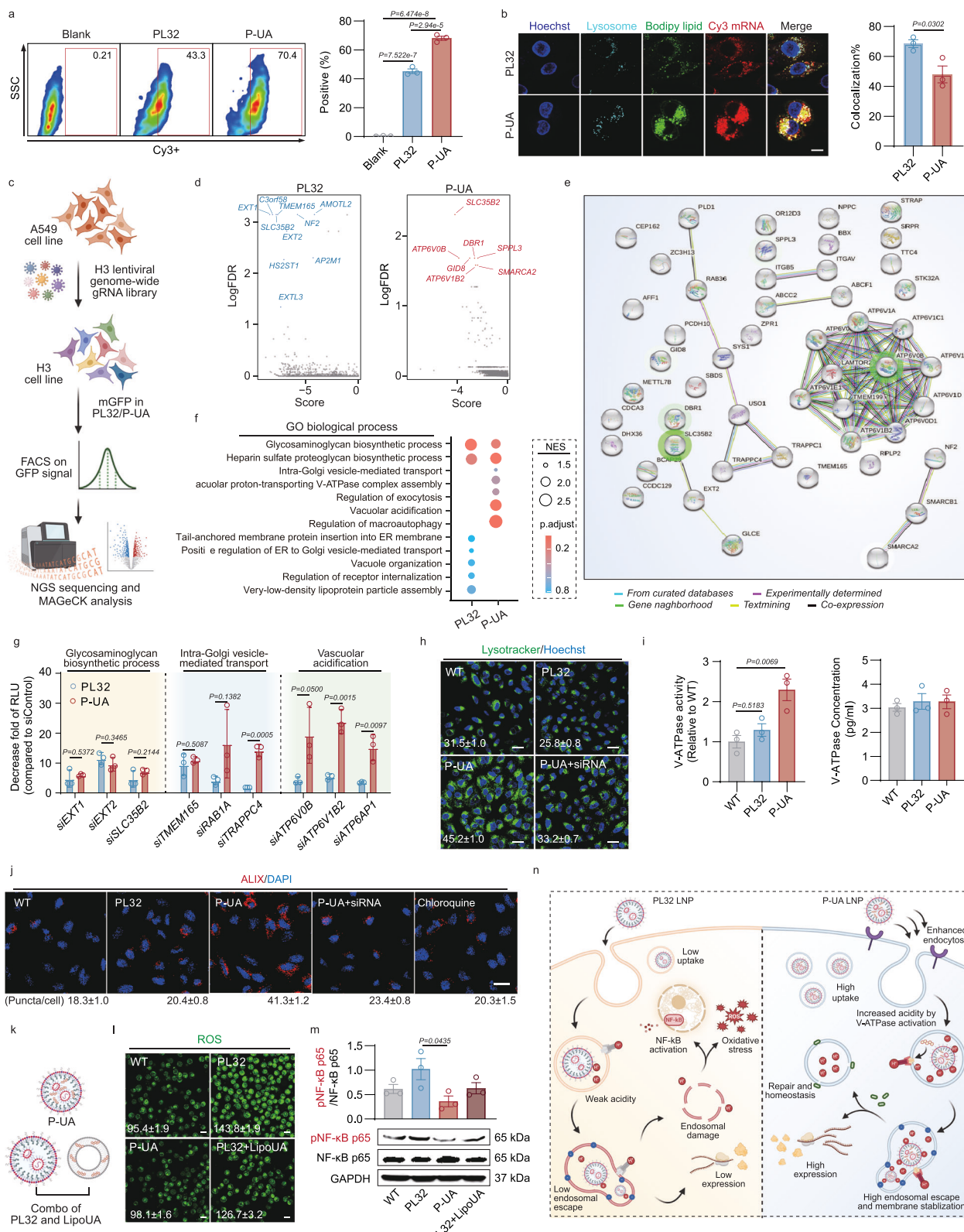
Generally, the inflammatory response induced by LNPs is dependent on the ionizable lipid and correlates positively with mRNA expression levels. However, P-U LNPs deviated from this trend by achieving high protein expression efficiency with minimal inflammation. To explore the potential mechanism behind this deviation, we first examined the cellular uptake and endosomal escape capabilities of PL32 LNPs and P-U LNPs using Cy3-labeled mLuc (Cy3-mLuc). Flow cytometry analysis revealed that P-U LNPs had significantly enhanced endocytic efficiency, with an increased cell positive rate of Cy3 from ~43% to ~70% (Fig. 3a). Additionally, we assessed the endosomal release kinetics of mRNA LNPs by triple labeling with BODIPY-lipid, Cy3-mLuc, and the Lysotracker that stains endosomes. Confocal microscopy at 2 h post incubation with A549 cells revealed marked dissociation of mRNA from Lysotracker in the P-U LNP treated group, indicating rapid disassembly and release of mRNA from endosomes (Fig. 3b). In contrast, about 70% of mRNA in the PL32 LNP treated group remained co-localized with endosomes.

To identify specific cell types responsible for the high mRNA expression for P-U LNP, we employed a genetically engineered mouse model with a loxP stop codon cassette upstream of a GFP-2A luciferase sequence. Cleavage by cre-recombinase (delivered by mRNA encoding Cre, mCre) enabled targeted cell expression of both luciferase and GFP. Flow cytometry results demonstrated that P-U LNP exhibited higher *in vivo* transfection efficiency compared to PL32 LNPs (Figures S11a–c and S12) across various cell types, with epithelial and immune cells identified as the main targets for both types of LNPs. This suggests that the enhanced expression attributed to UA is a universal effect rather than being cell-type specific, which is in line with Figure S5b.

Next, we developed a flow cytometry-based genome-wide CRISPR knockout (KO) screen to identify the pivotal genes that account for the variance in mRNA transfection efficiency observed between PL32 and P-U LNPs. To achieve this, A549 cells were transduced with an H3 lentivirus library encompassing a broad spectrum of guide RNAs (gRNAs), targeting over 18,000 distinct genes with a total of 117,587 unique gRNAs. Two passages following transduction, the cells were exposed to mGFP encapsulated within both PL32 and P-U LNPs for 24 h (Fig. 3c). Subsequently, the cells were stratified into four groups based on their GFP expression levels, ranging from low to high (Figure S11d). The MAGeCK-RRA approach was then applied to assess the disparity in sgRNA enrichment between the groups exhibiting high (Group IV) and low (Group I) GFP expression levels³⁸. The sgRNAs were subsequently ranked based on their enrichment in lower GFP groups, thereby identifying genes that function as positive regulators for both types of LNPs (Fig. 3c).

The top 70 genes that were enriched in the low expression groups of PL32 LNPs and P-U LNPs, in contrast to the high expression group were summarized in Supplementary data 1 and 2. Comprehensive analysis utilizing Gene Ontology (GO) (Fig. 3f), Kyoto Encyclopedia of Genes and Genomes (KEGG) (Figure S11h), and Reactome (Figure S11h), along with STRING-based protein interaction evaluations (Fig. 3e and Figure S11f), revealed that the genes involved in the glycosaminoglycan biosynthetic process and heparan sulfate proteoglycan biosynthetic pathways have a significant impact on the transfection efficiency for both PL32 LNPs and P-U LNPs (Fig. 3d–f and Figure S11e–h). These findings are in alignment with previous studies, which propose that the ionizable cationic liposomes interact with the negatively charged proteoglycans on the cell surface to facilitate nanoparticle internalization by pulmonary epithelial and endothelial cells³⁹. We further validated this hypothesis through the knockdown of three key genes—*EXT1*, *EXT2*, and *SLC35B2*—that are primarily involved in the biosynthesis of heparin sulfate. Our results indicate that these genes' knockdown resulted in diminished cellular uptake of both PL32 and P-U LNPs, which affected the expression of the encapsulated mRNA (Figure S11i, j and Fig. 3g). Additionally, genes related to the transport functions of the endoplasmic reticulum-Golgi apparatus (i.e., *TMEM165*), and those involved in tRNA biosynthesis, were identified to have an influence on the RNA expression facilitated by both PL32 and P-U LNPs (Figure S11i, j and Fig. 3g). This outcome is expected, as these processes are crucial for the mRNA translation and the overall mRNA expression efficiency.

Remarkably, we discovered that genes associated with vesicle acidification, such as *ATP6VOB* and *ATP6V1B2*, and those regulating vesicular trafficking, including *TRAPCC4*, specifically influenced the expression of mRNA mediated by P-U LNPs as compared to PL32 LNPs (Fig. 3d–f and Figure S11e–h). STRING-based protein interaction analysis revealed that among the top 50 differentially expressed genes, 11 are closely interacting and belong to the ATPase-coupled transmembrane transporter family (Fig. 3e). These genes utilize energy from ATP hydrolysis to transport protons from the cytoplasm into organelles, such as endosomes, affecting lysosome organization (Figure S11g), macroautophagy (Fig. 3f GO analysis), and vesicle recycling processes (Figure S11h KEGG and Reactome analysis)⁴⁰. To further investigate this, we conducted siRNA-mediated knockdown of *ATP6VOB* and *ATP6V1B2*, genes encoding subunits of the V-ATPase (KO efficiency in Figure S11i). Importantly, we found that the knockdown of these vesicle acidification-associated genes resulted in a significant downregulation of mLuc expression (over a 10-fold change) in P-U LNPs compared to PL32 LNPs (Fig. 3g). It is noteworthy that the gRNA for *ATP6API*, a component of the vacuolar ATPases and a surface receptor for prorenin, along with another surface protein TRAPCC4, were enriched in the low expression population. The knockdown of these membrane proteins led to a decrease in the uptake of P-U LNPs and the subsequent mLuc expression (Figure S11j and Fig. 3g), suggesting that these proteins are involved in the cellular uptake of P-U



LNPs. In summary, the siRNA knockdown studies are in concordance with the CRISPR screening results, underscoring the close relationship between V-ATPase activity and the enhanced transfection efficiency attributed to P-UA LNPs.

Previously the V-ATPase was known to regulate endosomal pH⁴¹, therefore we seek to investigate how PL32 and P-UA LNPs affect endosomal acidity. By employing the pH-sensitive dye

lysotracker in A549 cells, we detected a reduction in fluorescence intensity after treatment with PL32 LNPs (Fig. 3h). This decrease in fluorescence suggests a diminished endosomal acidity, which may be attributed to endosomal rupture triggered by the cationic charges present in PL32. On the other hand, P-UA LNPs were found to elevate endosomal acidity. This increase could potentially enhance the fusion process between ionizable cationic lipids and the

Fig. 3 | NIF LNPs improve mRNA expression and reduce inflammatory injury by activating V-ATPase. **a** Cellular uptake of Cy3-labeled PL32 and P-UA LNPs analyzed by flow cytometry ($n = 3$ wells). **b** Confocal images of intracellular distribution of LNPs in A549 cells. Three-time repeats with similar results. Scale bar, 20 μ m. **c** Schematics of genome-wide CRISPR knockout (KO) screen method. **d** Hits of the top 10 gRNAs enriched in the GFP-low population in PL32 and P-UA LNPs. **e** String-based protein interaction based on top 50 gRNAs enriched in the GFP-low population of P-UA LNPs. **f** Gene Ontology (GO) analysis of gRNAs in GFP-low population of P-UA LNP, p.adjust is calculated using Benjamini-Hochberg method. **g** Decreased folds of mLuc expression in major gene knockdown cell lines ($n = 3$ wells). **h** Endosomal acidity measured by lysotracker in different groups. A549 cells were treated with 200 ng of mLuc LNPs for 2 h. The relative fluorescence intensities from 3 parallel tests were quantified. Scale bar, 20 μ m. **i** V-ATPase activity and concentration evaluation in purified endosomes treated with LNPs for 24 h in A549 cells ($n = 3$ dishes). **j** IF staining of ALIX in A549 cells with different treatments. The

number of ALIX puncta per cell was shown below. Three-time repeats with similar results. Scale bar, 50 μ m. **k** Schematics of separate dosing of UA liposomes (LipoUA) with PL32 LNPs and P-UA LNPs. **l** ROS activation after treatment with LNPs and separate UA liposomes with PL32 LNPs in RAW264.7 cells. Three-time repeats with similar results. Scale bar, 10 μ m. **m** Downstream activation of NF- κ B pathways after treating with LNPs, and separate UA liposomes with PL32 LNPs in RAW264.7 cells ($n = 3$ wells). GAPDH: the loading control. **n** Schematics of the mechanism of UA promoting mRNA expression and reducing inflammation. Data were represented as mean \pm SEM. Statistical significance was calculated through two-tailed unpaired Student's t-test (**b**, **g**), One-way ANOVA with Dunnett's test (**i**) or Tukey's test (**a**, **m**). Figure 3c, **k**, **n** were created in BioRender. com with attribution line Miao, L. (2025) <https://BioRender.com/4huuyh8x>, Miao, L. (2025) <https://BioRender.com/4bfch5u> and Miao, L. (2025) <https://BioRender.com/nqlsk00>, respectively. Source data are provided as a Source Data file.

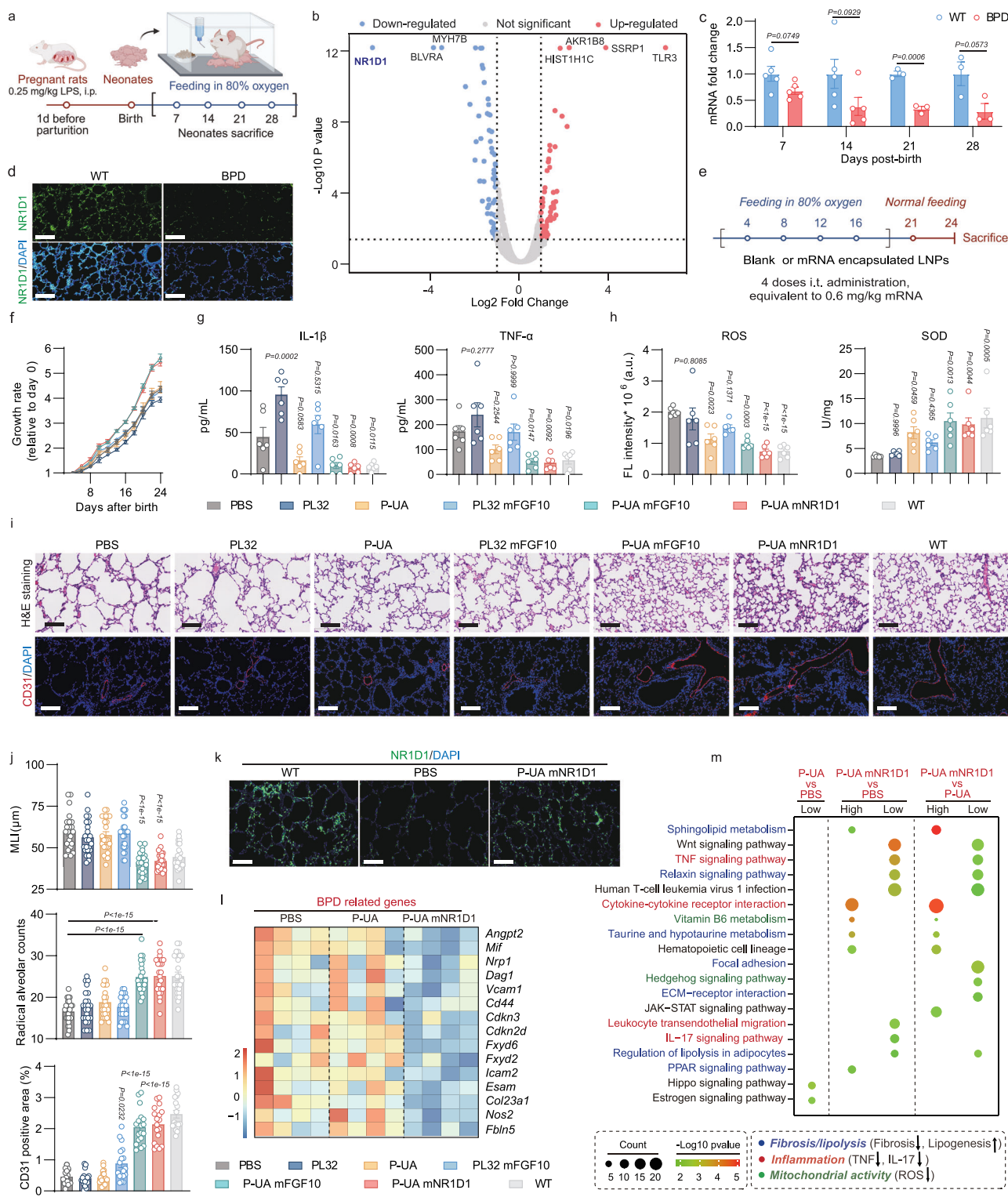
endosomal membrane, thereby facilitating the release of mRNA into the cytoplasm and preserving endosome homeostasis, as depicted in Fig. 3b.

To further investigate the mechanisms by which P-UA LNPs regulate endosomal pH and balance mRNA expression with immunogenicity, we first evaluated their impact on the activity and expression levels of V-ATPase. Our results indicate that P-UA LNPs did not significantly impact the endosomal V-ATPase level but potentially function as V-ATPase agonists, substantially enhancing the enzyme's activity (Fig. 3i). This enhancement aligns with the results of CRISPR knockout study, supporting our conclusion that the activation of V-ATPase by P-UA LNPs and the consequent acidification of endosomes are critical for the enhancement of protein expression. Moreover, V-ATPase-driven endosomal acidification is essential for maintaining endosome homeostasis^{41–43}. Previous studies have demonstrated that when endosomes experience minor ruptures accompanied by a slight dissipation of the pH gradient, Endosomal Sorting Complex Required for Transport (ESCRT) protein such as ALG-2-interacting protein X (ALIX) accumulate rapidly at the rupture site to promote their repair^{21,42}. In contrast, severe endosomal damage, characterized by large ruptures and a significant elevation of pH, fails to recruit ESCRT proteins^{21,42}. Building on the intrinsic role of V-ATPase in maintaining endosomal acidity, we hypothesized that acid-driven endosomal stability could mitigate membrane damage caused by LNPs. To verify our hypothesis, we investigated the recruitment of ALIX into endosomes after LNP treatment. Using chloroquine as a potent endosomal disruptor, we observed minimal to no ESCRT recruitment (indicated by minimal ALIX puncta). In contrast, treatment with P-UA LNPs resulted in significantly enhanced ESCRT recruitment compared to PL32 LNPs, suggesting the presence of small perforations (Fig. 3j)²¹, supporting our hypothesis. Furthermore, we knocked down *ATP6VOB* and *ATP6VIB2*, genes encoding subunits of the V-ATPase, and observed a marked reduction in endosomal acidity and ESCRT recruitment following gene knockdown (Fig. 3j). To confirm that the reduced recruitment of ESCRT is a result of severe endosomal damage, we measured the production of reactive oxygen species (ROS) after LNP treatment. Endosomal damage is typically associated with increased ROS generation⁴¹. Indeed, we observed an enhanced ROS level in the PL32 LNP group, while ROS levels were significantly reduced when UA was either encapsulated within PL32 LNPs or co-delivered with PL32 LNPs in liposome form (Fig. 3k, l). Furthermore, the activation of NF- κ B (Fig. 3m and Figures S13–15), a key mediator of inflammatory responses associated with cationic lipid, was attenuated by the inclusion of UA. Altogether, our findings suggest that P-UA LNPs act as potential V-ATPase agonists, maintaining endosomal homeostasis to mitigate inflammation from membrane perturbation while promoting LNP uptake, membrane fusion, and release through small ruptures. However, the mechanisms underlying UA-V-ATPase interactions and V-ATPase-ESCRT coordination require further investigation.

Additionally, we evaluated the impact of separately delivering UA liposomes and PL32 LNPs on protein expression and inflammation (Figure S11k–m). Although combining PL32 LNPs with UA liposomes reduced immunogenicity compared to PL32 LNPs alone—likely due to UA's direct anti-inflammatory effects—the immune response remained higher than that observed with co-encapsulated P-UA LNPs. Furthermore, UA liposomes alone failed to enhance protein expression relative to P32 LNPs in either in vitro or in vivo settings (Figure S11l, m), collectively demonstrating the superior efficacy of the single-vehicle P-UA formulation. Two potential explanations were considered for the inability of UA liposomes to improve PL32 LNP-mediated protein expression. First, liposomes might compete for cellular uptake receptors required for LNP internalization. Second, separate delivery could lead to UA liposomes and PL32 LNPs being sorted into distinct endosomes, thereby disrupting the synergistic V-ATPase-mediated coordination of mRNA release and inflammation relief. To evaluate this hypothesis, we compared P32 LNPs alone with P32 LNPs combined with blank liposomes. The latter combination resulted in decreased mRNA expression, which could only be partially rescued by separate UA liposome delivery (Figure S11l). In striking contrast, P-UA LNPs demonstrated optimal performance, showing the most significant enhancement in mRNA expression coupled with reduced immunogenicity (Figure S11k, l). These findings underscore the critical importance of co-delivery within a single nanoparticle system for achieving maximal benefit.

NIF P-UA LNP show improved efficiency in treating bronchopulmonary dysplasia

Bronchopulmonary dysplasia (BPD) is a severe lung condition affecting premature infants, leading to lasting impairments to lung function and neurodevelopment. Despite improvements in neonatal care that have increased survival rates, BPD's prevalence has risen^{44,45}. A key driver of BPD is the inflammatory response, which can worsen lung damage, emphasizing the importance of innovative therapeutic approaches to manage this condition⁴⁶. In this study, we employed a well-established hyperoxia/inflammatory-induced BPD rat model that demonstrates key pathological features mirroring clinical BPD manifestations in infants, particularly the characteristic alveolar simplification^{47–51}. As shown in Fig. 4a, b, we observed a significant downregulation of NR1D1, a circadian clock protein, compared to normoxic controls (Fig. 4a, b). NR1D1, crucial for regulating circadian rhythms, inflammation, oxidative stress, lung fibrosis, and mitigating lung injury⁵², showed a consistent downregulation at the mRNA level with extended hyperoxia exposure (Fig. 4c), with corresponding decreases in protein levels (Fig. 4d). To enhance NR1D1 expression directly within cells, we proposed mRNA therapy. In vitro validation on A549 cells demonstrated successful upregulation of NR1D1 and activation of downstream pathways after mNR1D1 delivery (Figure S16). Given the widespread decrease in NR1D1 across multiple lung cell types



in damaged tissue (Fig. 4d)⁵³, we explored the potential of P-UA LNPs as mRNA carriers for BPD treatment. P-UA LNPs showed a 9.3-fold increase in luciferase expression in the rat BPD lung compared to the original PL32 LNP (Figure S17a, b), indicating their potential as effective delivery vehicles for mNR1D1 therapeutics in BPD.

We further investigated the therapeutic potential of NR1D1 protein replacement therapy using P-UA LNPs encapsulating mNR1D1 for BPD in rats. FGF10, a growth factor that showed effective in BPD treatment, was used as a positive control (Fig. 4e)^{54,55}. Five therapeutic agents, including empty and RNA-loaded LNPs, were intratracheally

administered to BPD rats, with normoxia-exposed rats as controls. The BPD rats showed growth retardation compared to healthy rats. While empty LNPs and mFGF10-loaded PL32 LNPs had minimal effects, P-UA LNPs containing mFGF10 and mNR1D1 significantly promoted growth, with weight gains similar to healthy rats (Fig. 4f and Figure S17c). The empty PL32 LNPs induced a 1.4- to 4-fold upregulation of inflammatory cytokines, whereas empty P-UA LNPs relieved inflammation and oxidative stress by reducing inflammatory cytokines (IL-1 β , IL-6, CXCL1 and TNF- α), white blood cell (WBC) count, ROS levels and enhancing SOD activity (Fig. 4g, h, Figure S17d, e). The therapeutic effect on

Fig. 4 | NIF LNPs relieve lung injury in bronchopulmonary dysplasia (BPD) rat model. **a** Schematic representations of BPD models. **b** Proteomic differential analysis of lung tissues in BPD rats and wild-type (WT) rats ($n = 4$ rats). **c** Relative mRNA expression of *Nr1d1* in healthy and BPD rats with 80% oxygen exposure for different days ($n = 5$ rats in day 7 and 14, $n = 3$ rats in day 21 and 28). **d** Representative immunofluorescence staining of NR1D1 in lungs from healthy and BPD rats with 80% oxygen exposure for 21 days. **e** Treatment schedules for intratracheal administrations of PBS, blank and mRNA containing LNPs (equivalent to 0.6 mg/kg mRNA, blank LNPs with the same lipid dose). **f** Growth rate of BPD rats after different treatments ($n = 6$ rats). **g** Inflammatory cytokine levels in BAL and **(h)** reactive oxygen species (ROS) and superoxide dismutase (SOD) levels in lung tissues from BPD rats in all treatment groups ($n = 6$ rats). **i** H&E and CD31 staining of lungs in BPD rats with all groups after treatment. Scale bar, 100 μ m. ($n = 6$ rats in each group). **j** Mean linear intercept (MLI), radical alveolar counts (RACs) and CD31

coverage% area in rats' lung. The quantification was performed in four randomly selected fields per rat for MLI and RACs and three randomly selected fields for CD31 (from $n = 6$ rats). **k** IF staining of NR1D1 in the lungs from BPD rats treated with P-UA mNR1D1. Same experiments were repeated three times, with one representative image shown. Scale bar, 100 μ m. **l** Heat map and **(m)** bubble chart analyzed by KEGG showing the key altered pathways of the bulk transcriptome in lung of BPD rats treated with PBS, blank P-UA LNPs, and mNR1D1 LNPs ($n = 4$ rats in each group). Data were represented as mean \pm SEM. Statistical significance was calculated through two-tailed unpaired Student's t-test (**c**) or One-way ANOVA with Dunnett's test (**g, h, j**). Two side Fisher test was performed for **(m)**. Figure **(a, e)** were created in BioRender. com with attribution line Miao, L. (2025) <https://BioRender.com/mlpmmia> and Miao, L. (2025) <https://BioRender.com/86u5sda>, respectively. Source data are provided as a Source Data file.

inflammation was further enhanced with P-UA LNPs containing mFGF10 and mNR1D1. BPD rats exhibited characteristic alveolar simplification and decreased angiogenesis, which were effectively mitigated by P-UA LNPs loaded with mFGF10 and mNR1D1, restoring lung architecture to near-normal levels and showing superior efficacy over mNR1D1-containing PL32 LNPs (Fig. 4i, j and Figure S17f). The α -SMA level decreased after P-UA mNR1D1 treatment (Figure S17g, S18 and 19). The upregulated NR1D1 level after P-UA mNR1D1 treatment was also validated using IF (Fig. 4k).

Transcriptomics analysis of the lungs in BPD rats revealed that post-treatment with mNR1D1 P-UA LNPs modulated inflammatory pathways, including those involving *Il-17* and *Tnf- α* , and pathways related to ROS (Fig. 4l, m and Figure S20). In addition, mNR1D1 LNPs promoted angiogenesis, reduced myofibroblast-related gene expression, and increased lipid droplet formation, suggesting a shift from myofibroblasts to lipofibroblasts beneficial for lung microenvironment stability (Figure S20). As expected, the expression of BPD-related genes was reduced following mNR1D1 LNPs treatment (Fig. 4l)⁵⁰. As a result, P-UA LNP encapsulating mNR1D1 presents a promising therapeutic regimen for treating BPD.

NIF P-UA LNP show improved in treating pulmonary fibrosis

A previous study has shown that disruptions in the circadian rhythm can affect the progression of idiopathic pulmonary fibrosis (IPF), with NR1D1 playing a pivotal role in regulating fibroblast differentiation triggered by TGF- β ⁵³. Building on the established anti-fibrotic efficacy of NR1D1 in treating BPD (Figure S17g), as well as its potential in addressing cigarette smoke-induced pulmonary inflammation and fibrosis⁵⁶, we investigated the therapeutic potential of delivering mNR1D1 for IPF treatment using NIF LNPs.

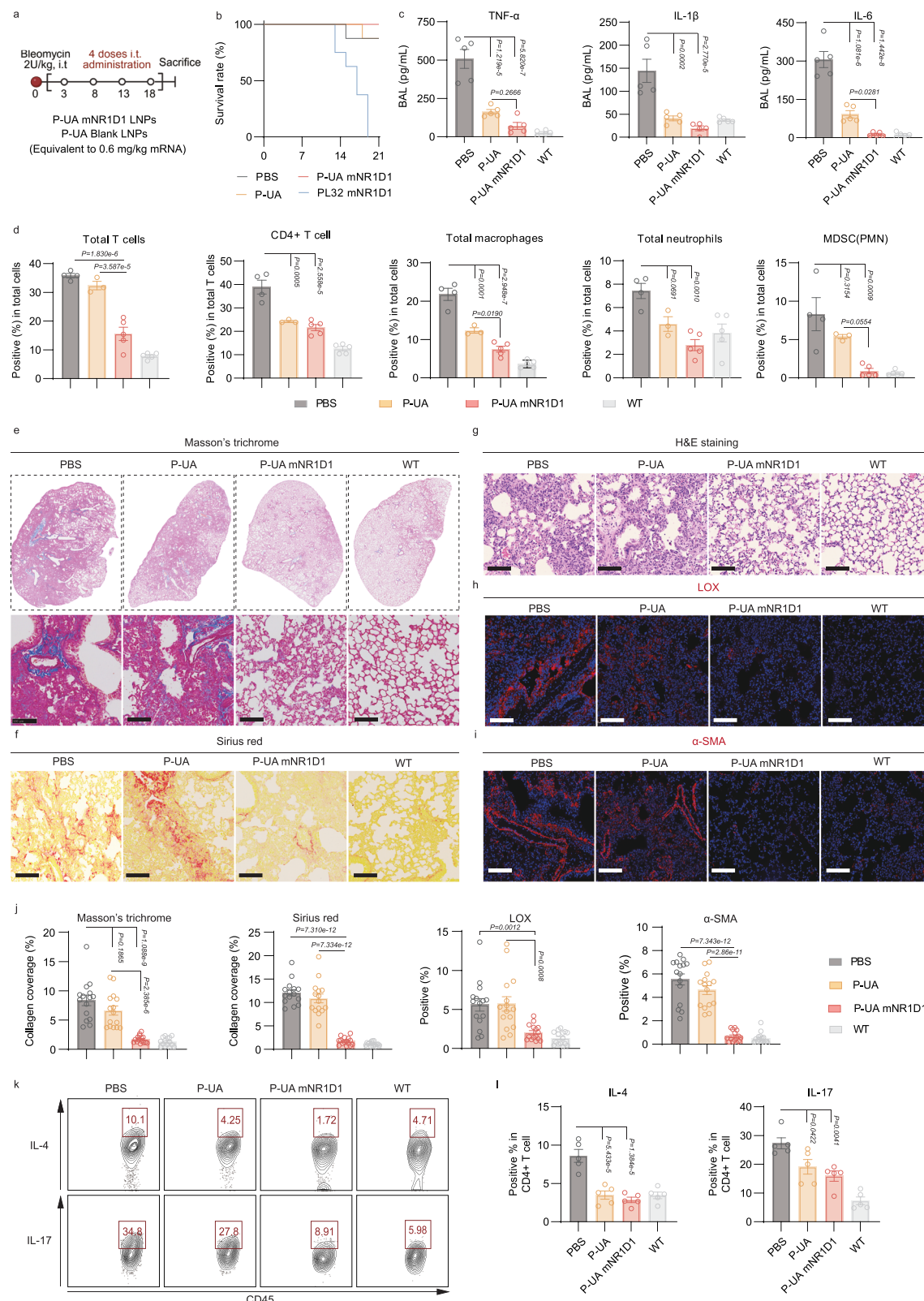
In line with the findings from healthy animals, we observed a 13.4-fold increase in luciferase expression in the IPF lungs following administration of P-UA LNPs compared to the original PL32 LNPs (Figure S21a and b). During establishing the IPF model, mice were intratracheally administered with PBS, empty P-UA LNPs, mNR1D1 PL32 LNPs, and mNR1D1 P-UA LNPs (Fig. 5a). Our results indicated that mNR1D1 delivered via inflammatory PL32 LNPs did not ameliorate IPF conditions, but instead resulted in significant mortality (Fig. 5b and Figure S21c). Conversely, empty P-UA LNPs significantly reduced pro-inflammatory cytokines by nearly 3-fold compared to the PBS-treated IPF group without causing any mortality (Fig. 5b and c). The inclusion of mNR1D1 in P-UA LNPs further enhanced the anti-inflammatory effect, leading to a 7- to 21-fold decrease in cytokine levels. Flow cytometry analysis revealed that mNR1D1 LNPs were more effective in curbing T cell infiltration and reducing macrophage and neutrophil levels compared to empty P-UA LNPs (Fig. 5d). Additionally, increased accumulation of monocyte-derived suppressor cells (MDSCs) in IPF lungs has been linked to the activation of lung fibroblasts^{57,58}. We observed that the levels of MDSCs were reduced to levels similar to the untreated group after treatment by mNR1D1 P-UA LNPs (Fig. 5d).

To further understand the function of NR1D1, we examined two proteins regulated by NR1D1, α -SMA and lysyl oxidase (LOX), and discovered that these proteins were significantly inhibited and the collagen I in their downstream was significantly decreased by mNR1D1 P-UA LNPs, not by the P-UA vehicle groups (Fig. 5h–j and Figure S21d). Consequently, this resulted in a remarkable anti-fibrotic effect, as evidenced by histological assessments using H&E, Masson's trichrome, and Sirius red staining (Fig. 5e–g, j). Given that NR1D1 is known to impact the function of TGF- β ⁴⁰, we observed a significant alleviation of CD4⁺ IL-17 and CD4⁺ IL-4 secreting cells, which have been shown to be regulated by TGF- β pathways (Fig. 5k, l)^{58–60}. Collectively, mNR1D1 encapsulated in non-inflammatory LNPs reduced both inflammation and fibrosis, effectively reversing IPF to a near-healthy state.

Process optimization of NIF LNPs for nebulization inhalation and freeze-dry to promote clinical feasibility

Nebulization is the main treatment route for neonates with BPD, and one of the most promising clinical administration routes for patients with IPF. Therefore, we explored the application of P-UA LNP via atomization for efficient delivery (Fig. 6a). However, we found that P-UA LNPs' protein expression significantly decreased after atomization due to aggregation, disintegration, and premature mRNA leakage caused by high shear forces (Fig. 6b). To enhance stability of LNPs during nebulization, we used sodium acetate (NaAc) as LNP buffer and hydrophilic polyethylene glycol (PEG6K and PEG20K) as stabilizing excipients as described elsewhere (Table S4)³⁰. While these modifications maintained particle size and mLuc encapsulation, they did not significantly improve post-nebulization protein expression (Fig. 6b and Figure S22a, b). We then hypothesized that the inherent surface charge of P-UA LNPs could help stabilize itself by electrostatic repulsion. Using a low-salt dialysis buffer, we enhanced the electrostatic repulsion by relieving charge shield of high ion concentration in PBS and improved atomization stability (Figure S22a). Notably, we found all three low salt buffers improved the encapsulation of mLuc within LNPs, increasing to approximately 85%, both prior and post nebulization (Figure S22a). Specifically, phosphate buffer-sucrose (PB-sucrose) low-salt dialysis buffer led to a 7.7-fold increase in protein expression, and without significant impacts on particle size post-nebulization compared to PBS-buffered P-UA LNPs (Fig. 6b, Figure S22a, b).

Since sucrose has been used as a lyoprotectant, we next proceeded to lyophilize the optimized LNP formulation. Following the lyophilization cycle shown in Figure S22c, all the P-UA LNPs exhibited a dense, white, and uniform freeze-dried cake appearance. Upon reconstitution with nuclease-free water, the lyophilized product demonstrated no discernible loss in protein expression (Fig. 6c, d and Figure S22d). Furthermore, after storage at 4 °C, the lyophilized vials retained their elegant cake structure, showing no signs of collapse, shrinkage or cracking. Post-reconstitution, the particle size and polydispersity remained stable for at least 3 months (Fig. 6e).



We next assessed the therapeutic efficacy of lyophilized and aerosolizable mNR1D1 P-UA LNPs in models of BPD and IPF via nebulization. We administered an adjusted dosage of 80 mg/kg of mNR1D1-encapsulated P-UA LNPs to BPD rats and IPF mice using a nebulization device (Figure S22e and g). Our results indicate that mNR1D1 P-UA LNPs effectively alleviated BPD in rats and IPF in mice, with a significant decrease in alveolar simplification and collagen

deposition (Fig. 6f-k, Figure S22f and h). Importantly, in beagle dogs that have a respiratory system similar to human's, mLuc-loaded P-UA LNPs showed over a 5-fold increase in lung protein expression compared to PL32 LNPs (Fig. 6l and m). Consistent with the study in mice and rats, P-UA LNPs were associated with significantly reduced inflammation, as indicated by decreased WBC counts and neutrophil proportions in the blood, lower levels of inflammatory cytokines and

Fig. 5 | NIF LNPs relieve lung injury in IPF mice model. **a** Treatment schedules for intratracheal administrations of PBS, PL32 LNPs formulated mNRID1, P-UA LNPs formulated mNRID1 (0.6 mg/kg), and empty P-UA LNPs with the same lipid dose. **b** Mice survival curve of all treatment groups and mNRID1 PL32 LNPs after 4 doses (0.6 mg/kg, $n = 8$ mice). **c** Inflammatory cytokine levels in BAL from IPF mice in all treatment groups ($n = 5$ mice). **d** Infiltrated immune cells proportion in the lung tissue of all treatment group by flow cytometry ($n = 4$ mice in PBS, $n = 3$ mice in P-UA, $n = 5$ mice in P-UA mNRID1 and WT group). T cells were labeled as CD45⁺CD11b⁻CD3⁺; CD4 T cells were labeled as CD45⁺CD11b⁻CD3⁺CD4⁺; macrophages were labeled as CD45⁺CD11b⁺F4/80high; neutrophils were labeled as CD45⁺CD11b⁺F4/80medLy6G⁺; polymorphonuclear myeloid derived suppressor

cells (MDSCs (PMN)) were labeled as CD45⁺CD11b⁺F4/80lowLy6clowLy6G⁺; (e) Representative images of Masson's trichrome, (f) Sirius red, (g) H&E, and IF staining of (h) lysyl oxidase (LOX) and (i) α -SMA in IPF mice after different treatments ($n = 5$ mice). Scale bar=100 μ m in (e–i). **j** The quantification of (e, f, h, i) was performed in three randomly selected fields per mouse (from $n = 5$ biological independent mice per group, mean \pm SEM). **k** Flow cytometric analysis of IL-4 (upper) and IL-17 (bottom) positive cells in CD45⁺ group ($n = 5$ mice). **l** Quantification of (k) ($n = 5$ mice). Data were represented as mean \pm SEM. Statistical significance was calculated through One-way ANOVA with Tukey's test (c, d, j, l). Figure 5a was created in BioRender. com with attribution line Miao, L. (2025) <https://BioRender.com/sbg9i5w>. Source data are provided as a Source Data file.

C-reactive protein (CRP) and reduced immune cell infiltration in blood, BAL, and lung (Fig. 6n-p and Figure S22i). Altogether, we optimized the preparation process to allow P-UA LNPs for nebulization administration and long-term freeze-dried storage, greatly enhancing their clinical translational potential.

Discussion

LNP-based mRNA therapies are emerging as treatments for a range of diseases, yet they face major challenges such as inflammation and inadequate protein expression. In our study, we designed a series of biodegradable, ionizable cationic lipids, known as PLs, with a piperazine-centered phosphoramido core for efficient lung mRNA delivery. The lead lipid, PL32, showed high protein expression but also induced significant immunogenicity. We noticed a positive correlation between protein expression levels and immunogenicity in both tested PL LNPs and commercial LNPs.

To counteract these issues, we integrated PLs with NAIPs to craft LNPs that could reduce inflammation and boost protein expression. NAIPs are advantageous as they have fewer side effects than conventional anti-inflammatory medications. Through our screening, we found that UA, a pentacyclic triterpenoid, when included in the LNP formulation, significantly increased lung protein expression without causing substantial reactogenicity in various species, including mice, rats, dogs, and human PBMCs. Notably, even high doses of P-UA LNPs did not worsen inflammation in ALI and IPF models, suggesting their suitability for mRNA therapy in inflammatory lung diseases. To enhance the applicability of our method, we optimized the P-UA LNP preparation by using low salt and sucrose as dialysis medium, which improved stability during atomization and freeze-drying. These optimized LNPs remained stable for three months and successfully delivered mLuc to beagle lungs via inhalation.

Using a genome-wide CRISPR knockout platform, we unraveled the intricate mechanisms by which P-UA LNPs regulate mRNA expression and immunogenicity, revealing an important role for V-ATPase in this process. Unlike traditional LNP formulations (e.g., PL32), which reduce endosomal acidity due to their multi-tertiary amine head groups and induce endosomal membrane damage—likely through the formation of “large ruptures”—triggering inflammation via NF- κ B and ROS pathways, P-UA LNPs uniquely enhance endosomal acidification by activating V-ATPase. This activation promotes membrane homeostasis and enables a more controlled and efficient release of LNPs, likely through the formation of “small ruptures.” This mechanism, combined with ESCRT-mediated endosomal repair, significantly reduces inflammation. Furthermore, the lowered endosomal pH enhances the charge potential of LNPs, facilitating membrane fusion and endosomal escape, thereby achieving an optimal balance between mRNA expression and reactogenicity.

While direct interactions between V-ATPase and ESCRT remain underexplored, emerging evidence suggests a potential link, as pH gradient changes during ESCRT recruitment and the role of endosomal lipid phosphatidylinositol in ESCRT O recruitment and V-ATPase localization imply functional crosstalk^{61,62}. Further investigation is needed to elucidate the precise mechanisms, including whether the

interactions between UA and V-ATPase, as well as V-ATPase and ESCRT, are direct or indirect. These findings highlight the innovative potential of P-UA LNPs in optimizing LNP delivery systems while minimizing immunogenicity, offering a generalized approach of involving V-ATPase modulation in LNP delivery.

This study also evaluated the potential of non-inflammatory LNPs in delivering therapeutic mRNA to treat BPD and IPF diseases, marked by chronic inflammation. In BPD, where no approved therapies exist, we identified NRID1, a transcriptional repressor and circadian clock regulator, as a promising target. Our study also demonstrated the potential of delivering an intracellular nuclear receptor for therapy. We showed that mNRID1 P-UA LNPs could effectively treat BPD by reducing inflammation and oxidative stress, promoting fibroblast cell transformation, and enhancing angiogenesis. Moreover, mNRID1 P-UA LNPs showed significant anti-fibrotic effects in IPF models by normalizing collagen and lysyl oxidase expression. Conversely, conventional mNRID1 PL32 LNP treatment caused the death of IPF mice, highlighting the necessity of regulating LNP inflammation.

In conclusion, the development of freeze-dried, atomized, non-inflammatory P-UA LNPs in this study provides a promising mRNA therapy for treating inflammatory lung diseases by overcoming the typical trade-off between protein expression and reactogenicity. This approach underscores the importance of endosomal homeostasis in improving therapeutic outcomes. Further studies are necessary to explore the UA-V-ATPase interaction and the broader potential of NIF-LNP strategy.

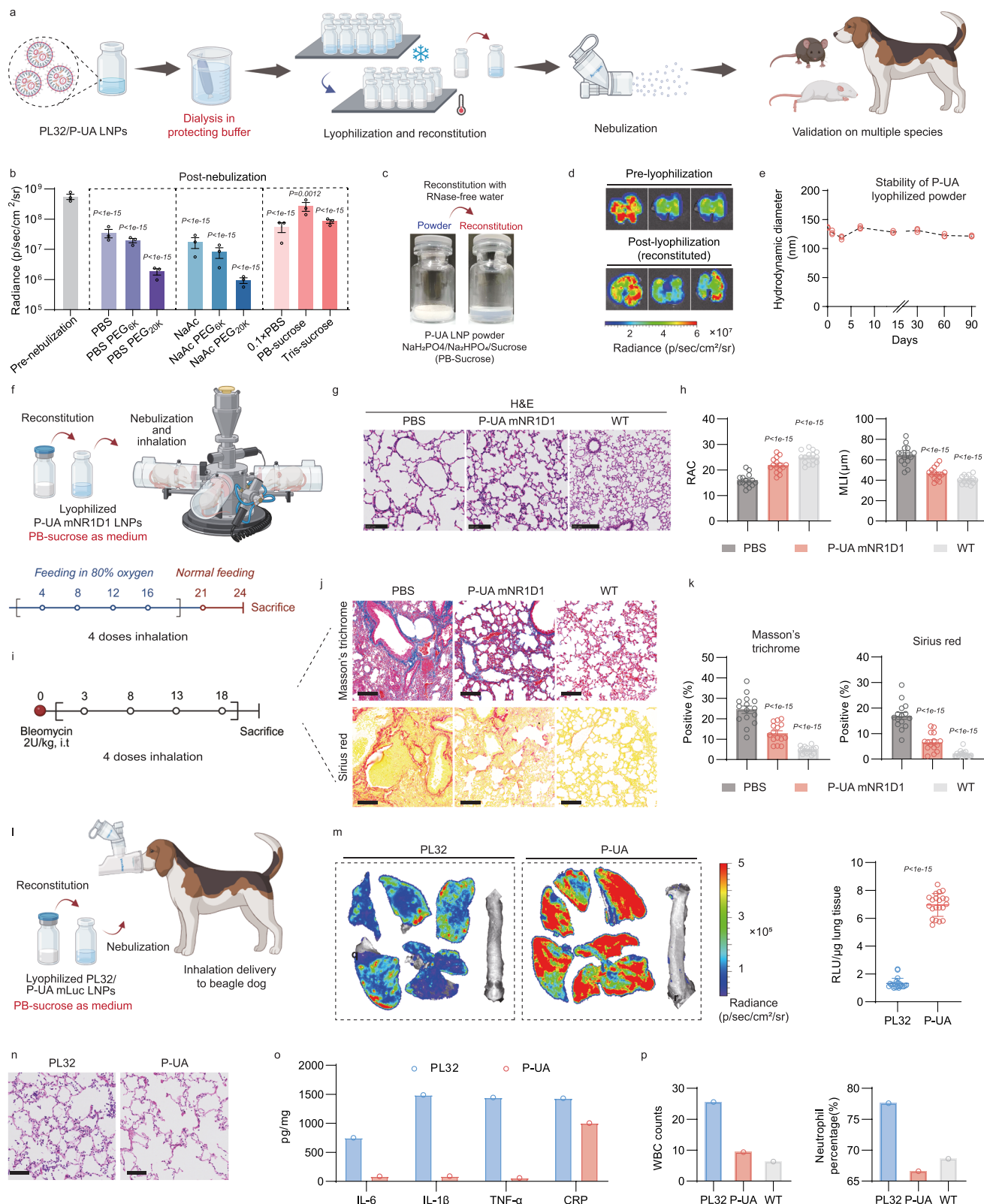
Methods

Ethical statement

Our research complies with all relevant ethical regulations. All animal research was in compliance with ethical regulations approved by Peking University's Institutional Animal Care and Use Committee for using mice (DLASBD0620), Animal Care and Use Committee of Peking University People's Hospital for using rats (2021PHE085), and the Animal Ethics Committee of Beijing Animals Science Biotechnology Co., Ltd. for beagle dogs (IACUC-AMSS-20240410-02).

Materials

Commercial ionizable lipids containing DLin-MC3-DMA (MC3) and 6-((2-hexyldecanoyl)oxy)-N-(6-((2-hexyldecanoyl)oxy)hexyl)-N-(4-hydroxybutyl)hexan-1-aminium (ALC-0315) were purchased from Avanti Polar Lipids, Inc. 2,5-Piperazinedione, 3,6-bis[4-[bis(2-hydroxydodecyl)amino]butyl] (cKK-E12) was purchased from MedChemExpress (MCE) Life Science Reagents. Helper lipids containing cholesterol, 1,2-Dioctadecanoyl-sn-glycero-3-phosphocholine (DSPC) and 1,2-dimyristoyl-rac-glycero-3-methoxypolyethylene glycol-2000 (DMG-PEG₂₀₀₀) were bought from AVT (Shanghai) Pharmaceutical Tech Co., Ltd. 1,2-dioleoyl-sn-glycero-3-phosphoethanolamine (DOPE) were purchased from Avanti Polar Lipids, Inc. All commercially purchased lipids were of analytical grade. Anti-inflammatory natural products were kindly gifted by Prof. Xue Qiao. Firefly luciferase mRNA (mLuc) was provided by Proxybio. All the plasmid sequences were provided by Genscript Co.,Ltd. Primers and siRNA were from Tsingke



Biotechnology Co., Ltd. HUVEC, HULEC-5a, AT-II cell and BEAS-2B cell line and their complete culture medium were purchased from Zhejiang Meisen Cell Technology Co., Ltd. Other cell lines and fetal bovine serum (FBS) were purchased from Procell Life Science & Technology Co., Ltd. Other reagents for basal culture were bought from Meilunbio Co., Ltd. ELISA kits for mouse IL-6, TNF- α , IL-1 β and IFN- γ and rat IL-1 β , IL-6, TNF- α and CXCL1 were purchased from Solarbio Science &

Technology Co., Ltd. Micro Fluidic for preparation of LNPs was provided from Micro&Nano Biologics Co., Ltd. The freeze dryer used in this study is LyoBeta-15 II 050-359 made in Telstar Co., Ltd.

mNR1D1, mFGF10 and mCre were synthesized using T7 polymerase mediated in vitro transcription (IVT) system from linearized pUC57 plasmid vectors containing T7 promoter, 5' and 3' untranslated regions (UTRs) and a poly A tail (100 nt). The clean-cap AG 5'

Fig. 6 | Preparation of aerosolizable and freeze-dried stable NIF LNPs.

a Schematics for LNP preparation, freeze-dried storage and reconstitution for nebulization inhalation. **b** Quantification of protein expression in lungs treated with P-UA LNPs of all formulations at 6 h post-administration by nebulization inhalation. ($n = 3$ mice, 0.2 mLuc/kg). **c** The photos of optimized P-UA LNPs after lyophilization and reconstitution. **d** IVIS images of lung in mice treated with mLUC P-UA LNPs pre- and post-lyophilization ($n = 3$ mice, 0.2 mLuc/kg). **e** Hydrodynamic diameter of P-UA LNPs post-lyophilization over 3 months ($n = 3$ independent tests). **f** Therapeutic schedule for BPD rats treated with mNRID1 P-UA LNPs by nebulization inhalation. **g** H&E staining of BPD lung treated with mNRID1 P-UA LNPs by nebulization inhalation ($n = 3$ mice). Scale bar, 100 μ m. **h** Quantification of radial alveolar count (RAC) and mean linear intercept (MLI) ($n = 3$ mice, five randomly fields each). **i** Therapeutic schedule for IPF mice treated with mNRID1 P-UA LNPs by nebulization inhalation. **j** Masson's trichrome and Sirius red staining of IPF lungs treated with mNRID1 P-UA LNPs by nebulization inhalation ($n = 3$). Scale bar,

100 μ m. **k** Quantification of coverage area of collagen ($n = 3$ mice, five selected fields each). **l** Schematics of mLUC expression of nebulized LNPs in beagle dogs. **m** IVIS images of dogs' lungs in treated with mLUC containing LNPs by nebulization inhalation (0.3 mg/kg). Quantification was presented on the right. 21 pieces of lung tissue from 7-lobe lung per dog were lysed for luminescence detection. **n** H&E staining of dogs' lungs treated with LNPs by nebulization inhalation. Scale bar, 100 μ m. **o** Cytokines in dogs' BAL after treated with LNPs by nebulization inhalation ($n = 1$ dog). **p** Neutrophils and WBC in dogs' blood after treated with LNPs by nebulization inhalation ($n = 1$ dog). Data were represented as mean \pm SEM. Statistical significance was calculated through two-tailed unpaired Student's t-test (**m**) or One-way ANOVA with Dunnett's test (**b, h, k**). Figure 6a, f, i, l were created in BioRender. com with attribution line Miao, L. (2025) <https://BioRender.com/9yumzcs>, Miao, L. (2025) <https://BioRender.com/4flxdkv>, Miao, L. (2025) <https://BioRender.com/6wt8ggy> and Miao, L. (2025) <https://BioRender.com/scwelol>, respectively. Source data are provided as a Source Data file.

capping (Cap 1) and 1-methylpseudo-uridine UTP were added to the transcription reaction. The uridine-5'-triphosphate (UTP) was fully replaced with 1-methylpseudo-uridine UTP. IVT reactions were conducted according to the manufacturers' protocols (Hongene Biotech Inc., China).

Lipid nanoparticle preparation and characterization

The mRNA containing aqueous solution and the ethanolic solution composed of ionizable lipid, DSPC, cholesterol, DMG-PEG₂₀₀₀ and natural products were mixed at a ratio of 3:1 by microfluidics to prepare LNPs. The formulations were displayed in Table S1. The organic solvent was removed by dialyzing with dialysis bag (14 kDa cut off) in phosphate buffer saline (1× PBS, over 1000-fold to LNP volume) at 4 °C overnight.

For nebulized administration, LNPs were dialyzed (14 kDa cut off) in 1×PBS, 0.1×PBS, phosphate buffer sucrose, tris buffer sucrose and NaAc buffer (over 1000-fold to LNP volume). 2% w/v excipients were added in each LNP formulations. Detailed prescription and preparation process were summarized in Table S4. Then, 500 μ L of dialyzed LNPs were loaded into an Aeroneb vibrating mesh nebulizer placed on ice and condensate LNPs were collected into 1.5 mL microcentrifuge tubes.

mRNA concentration and encapsulation efficiency of LNP were measured using Quant-it RiboGreen RNA assay (Invitrogen). The hydrodynamic diameter and zeta potential of LNPs were measured in 1×PBS and 4 mM KCl using dynamic light scattering (Zetasizer Nano ZSP, Malvern).

UA liposome preparation

Ethanol injection method was used for liposome preparation. Briefly, DSPC, cholesterol and UA were mixed with 15:5:1.5 mass ratio as organic phase. Then, 200 μ L organic phase was mixed with 600 μ L pure water. Ethanol was removed by overnight dialysis in PBS.

Cells culture and assays

A549 lung epithelial cells were maintained in RPMI-1640 medium supplemented with 10% fetal bovine serum (FBS, Procell, China) and penicillin, streptomycin (Meilunbio, China). RAW 264.7 were maintained heat inactivated DMEM medium. HUVEC-5A were maintained in DMEM medium, with 10%FBS,1% Anti-Anti. BEAS-2B were maintained in BEGM (bronchial epithelial cell growth medium). AT2 were maintained in DMEM medium with 10 ng/ml hEGF, 5ug/ml insulin and 10%FBS,1% Anti-Anti. HUVEC were maintained in complete culture medium for HUVEC from Wuhan Pricella Biotechnology Co., Ltd.

In vitro inflammation detection of Empty LNPs

Empty LNPs were prepared by the above-mentioned method without adding mRNA to aqueous phase. RAW 264.7 macrophages of 5×10^4 per well were seeded in 24-well plates overnight and IFN- γ (2.5 ng/mL)

and LPS (200 ng/mL) were added for 12 h to induce macrophage differentiation into M1 type. Then, 10 μ L of empty LNPs were added to cells for 24 h. The cells were lysed by Trizol and RNA were extracted for qPCR assay.

Quantitative real-time PCR (qPCR) assay

The RNA of lung tissue and cultured cells were extracted and purified using the TransZol Up Plus RNA Kit (TransGen Biotech). cDNA was reverse-transcribed by HiScript III All-in-one reverse transcription (RT) SuperMix Perfect for qPCR (Vazyme Biotech Co., Ltd). qPCR was performed by Sybr green method using qPCR SuperMix (TransGen Biotech) on QuantStudio™ 6 Flex with QuantStudio Real-Time PCR Software v1.7.1. All the primers are listed in Table S6. glyceraldehyde-3-phosphate dehydrogenase (GAPDH) was applied as endogenous control. The quantification was conducted as $2^{-\Delta\Delta Ct}$ value.

In vitro transfection

For Luc protein transfection, cells of 10^4 per well were seeded in 96-well plates overnight and mLUC containing LNPs were added to cells at 0.1 μ g mLUC per well. Twenty-four h later, the transfection efficiency was measured by Firefly-Glo Luciferase Reporter Assay Kit (Yeasen Biotechnology Co., Ltd.) following the manufacturer's protocol, using BioTek synergy H1 microplate reader.

For GFP protein transfection, cells of 10^4 per well were seeded in 96-well plates overnight at 10^4 cells per well and mGFP containing LNPs were added to cells at 0.1 μ g, 0.2 and 0.4 μ g mRNA per well. Four hours later, LNPs were removed, and fresh culture medium was supplemented. At 24 h, fluorescence signal of GFP protein was measured by flow cytometer.

Cytokine measurements in PBMC

Human peripheral blood mononuclear cells (PBMCs) were purchased from Milestone (PBLP-08B). PBMCs of 1×10^5 per well were plated in 96-well plates, and then LNPs were added at 1 μ g RNA per well. After 24 h, cells were centrifuged for 3 min (500 g) at 4 °C and the supernatant is collected. The cytokines including IL-1 β , IL-2, IL-4, IL-6, IL-8, TNF- α and IFN- γ were measured by human inflammatory cytokine cytometric bead array (CBA) - 1 kit according to manufacturer's instructions.

In vitro cell uptake

A549 cells were plated in 96-well plates at a density of $\sim 10^4$ cells per well 24 h prior to the experiment. siRNA containing LNP with the formulation of MC3 were used for the knockdown of the related proteins. MC3 LNPs (siRNA) were added to cells at 200 nM at 37 °C 48 hours prior to LNP incubation. After pre-incubation of the LNPs, the supernatant was aspirated and washed twice with PBS. Then, PL32 LNPs and P-UA LNPs encapsulated with Cy3-mLuc (equivalent to 0.1 μ g RNA per well) were added into each well of cells. After 2 h of incubation at 37 °C,

the wells were washed 3 times with cold PBS and replaced with fresh media. The cellular uptake was determined by flow cytometry.

Live-cell imaging of mRNA release

Intracellular release of mRNA from LNPs was visualized using an inverted Zeiss LSM880 confocal microscope. Airyscan array detector unit (Carl Zeiss AG) was used to strengthen and visualize the cytosol Cy3-mLuc signals within the live cells. Five % BODIPY-lipid and Cy3-mLuc were applied for tracing the intracellular behavior of LNP and mRNA. A549 cells were plated in 96-well plates at a density of $\sim 10^4$ cells per well 24 h prior to the experiment. Cells were treated with the labeled LNP with mRNA at a concentration of 1 $\mu\text{g}/\text{mL}$ and incubated for 2 hours at 37 °C. Subsequently, the media were replaced with fresh media containing 1 $\mu\text{g}/\text{mL}$ of Hoechst 33342 and lysotracker, and endosome release was observed using a 100 \times Plan-Neofluar 1.3 numerical aperture (NA) oil-immersion objective. For all experiments, the field of view (FOV) was set to 354, 25 $\mu\text{m} \times 354$, 25 μm (full). The pinhole was set to 1 Airy Unit (AU) for all channels. The acquired imaging data were processed using Zen2.3 software (blue edition) for analysis. The colocalization of the fluorescent signals of Cy3-mLuc and lysotracker was quantified using the Pearson correlation coefficient (PCC) implemented in the ImageJ 1.53 u.

Pooled genome-wide CRISPR screening of P32 and P-UA LNP

A genome-wide H3 human CRISPR KO library targeting >18,000 genes (a total of 117,587 sgRNAs) in pLentiCRISPRv2 vector was obtained from Addgene (#133914). Plasmid amplifying and viral packaging were performed following the published protocols provided for maintaining library representation^{63–66}. ~200 million A549 cells were seeded into 15 cm dishes (~14 million cells per dish) each containing 25 mL complete RPMI 1640 (RPMI 1640 with 10 v/v% FBS and 1 v/v% penicillin/streptomycin) and incubate overnight in 37 °C, 5% CO₂ incubation for cell adhering. Next morning, polybrene and H3 lentivirus library was added into the dishes. The final concentration of polybrene was 8 $\mu\text{g}/\text{mL}$ and the volume of lentivirus added was determined by titrating the virus in identical conditions to infect roughly 24% of cells, which is standard in lentiviral genome-wide knockout screens to ensure that most cells being infected by a single virus. Twenty-four hours after infection, viral media was removed from the dishes and replaced with fresh complete media. The cells were incubated for another 24 h to allow puromycin resistance gene expression, and then 2 $\mu\text{g}/\text{mL}$ puromycin was added to select for infected cells. Three days after puromycin selection, all of the remaining cells were collected and pooled together to get A549-H3 library cell line. A549-H3 cells were cultured in 25 mL complete RPMI 1640 medium per dish with 1 $\mu\text{g}/\text{mL}$ puromycin and passaged every 2–3 days, with at least 30 million cells retained each passage for maintaining library representation.

A549-H3 cells were propagated approximately two generations to achieve a stable CRISPR KO phenotype. Then the cells were pooled together and split into three replicates (~30 million cells per replicate, ~14 million cells per 15 cm dish), one of which as the unsorted control for quality check and the other two groups were transfected with P32 or P-UA LNP loading mGFP respectively at a dose of 3 μg mGFP per dish. Twenty-four hours after the transfection, the cells were collected and sorted based on EGFP expression using FACS. We isolated the lowest and highest 10–15% of expressing cells for each group and extracted the genomic DNA together with the unsorted control using TIANamp Genomic DNA Kit (Tiangen #DP304).

The sgRNA barcodes were PCR amplified from the genomic DNA with 2 \times EasyTaq® PCR SuperMix (TransGen #AS11-11) by three rounds following the published protocols^{63–66}. 1st round of PCR amplifies up a sequence from the U6 promoter to the EF1a promoter spanning the gRNA sequence on the modified pLentiCRISPRv2 backbone; 2nd round of PCR uses pairs of F + R primers to add 8-nt index to each sample for multiplexing and increase base diversity at each Illumina sequencing

cycle; and 3rd round of PCR primers equals Illumina P5 and P7 adaptors. All of the primer sequences used were listed in Table S5. The third PCR products were gel-purified using TIANgel Purification Kit (Tiangen #DP219) and submitted to Sequanta Technologies Corporation for sequencing. Amplicon libraries were sequenced with Illumina NovaS4. Data analysis was performed using MAGeCK version 0.5.9.3, as reported in our previous publication^{63–66}, to carry out quality control and detect differentially enriched genes and pathways between low- and high-expression groups. The p.adjust is calculated using the Benjamini-Hochberg (BH) method, which controls the false discovery rate (FDR) by ranking raw p-values and adjusting them to reduce false positives in genome-wide CRISPR screen results.

Detecting acidity of the endosomal compartment

A549 cells were plated in 8-well plates at a density of $\sim 2 \times 10^4$ cells per well 24 h prior to the experiment. The siRNA (ATP6VOB and ATP6V1B2) containing LNPs with the formulation of MC3 were used for the knockdown of the V-ATPase related proteins. MC3 LNPs (containing siRNA) were added to cells with 200 nM at 37 °C for 48 h prior to LNP incubation. Then, cells were treated with LNPs with mLuc at a concentration of 2 $\mu\text{g}/\text{mL}$ and incubated for 30 min at 37 °C. Subsequently, the media were replaced with fresh media containing 1 $\mu\text{g}/\text{mL}$ of Hoechst 33342 and lysotracker. Confocal microscope was used for detecting the lysotracker signal in cells.

Measurement of V-ATPase concentration and activity in vitro

Cells of $\sim 5 \times 10^6$ per 15 cm dish were treated with LNPs with mLuc at a concentration of 1 $\mu\text{g}/\text{mL}$ and incubated for 24 h at 37 °C. Endosomes were purified using an endosome extraction Kit according to manufacturer's method. Briefly, the cells were harvested by centrifugation (850 \times g, 2 min, 4 °C) and homogenized on ice using a Dounce homogenizer. Cellular debris and organelles were subsequently removed using a commercial endosome extraction kit. The isolated endosomes were washed three times with PBS to remove residual contaminants. The roughly extracted endosomes were further isolated through density gradient centrifugation at 145,000 \times g for 2 h at 4 °C. The harvested endosomes were subsequently washed three times. The concentration of V-ATPase was evaluated by ELISA according to manufacturer's method. ATP hydrolysis activity was measured using a coupled spectrophotometric method as previously described⁶⁷. In brief, endosomes were suspended in ATPase assay buffer (50 mM NaCl, 30 mM KCl, 20 mM HEPES-NaOH, pH 7.0, 10% (v/v) glycerol, 1 mM MgCl₂, 1.5 mM phosphoenolpyruvate, 0.35 mM NADH, 20 U ml⁻¹ pyruvate kinase and 10 U ml⁻¹ lactate dehydrogenase) with 5 μM concanamycin A (for calculating V-ATPase-specific ATP hydrolysis activity) or DMSO, and pre-warmed at 37 °C for 10 min. The assay was initiated by the addition of 5 mM ATP, and the OD341 was continuously recorded by a BioTek synergy H1 microplate reader.

ALIX puncta imaging

A549 cells were plated in 24-well plates at a density of $\sim 5 \times 10^4$ cells per well 24 h prior to the experiment. After LNP with mLuc at a concentration of 1 $\mu\text{g}/\text{mL}$ and chloroquine (60 μM) treatments for 30 min at 37 °C, cells were fixed in 4% fresh paraformaldehyde for 15 min. For siRNA knockdown group, cells were treated with siRNA containing MC3 LNPs with 200 nM at 37 °C for 48 h prior to LNP incubation. Then, samples were incubated with 5% BSA for 1 h. After PBS washing, cells were cocultured with 1:250 primary antibodies at 4 °C overnight. Unbound antibodies were washed with PBS three times. Next, 1:1000 secondary antibodies were added to cells and incubated at 37 °C for 1.5 h. Unbound antibodies were washed with PBS three times. Cell nuclei were labeled by DAPI. Images were acquired by Vectra Polaris with Phenochart 1.0.8 software (Akoya, USA). Quantitative results were showed by the number of ALIX puncta per cell per image. ($n=3$ in each group)

ROS detection

RAW264.7 cells were plated in 24-well plates at a density of $\sim 5 \times 10^4$ cells per well 24 h prior to the experiment and were treated with LNPs or LNPs + UA liposomes with mLuc at a concentration of 2 $\mu\text{g}/\text{mL}$ and incubated for 4 h at 37 °C. Dihydroethidium (DHE) probe was loaded in cells and incubated for 30 min at 37 °C. Confocal microscope were used for detecting the ROS signal.

Western blot

For cell sample, the cells were plated in 24-well plates at a density of $\sim 5 \times 10^4$ cells per well 24 h prior to the experiment. For tissue sample, ~ 20 mg tissue was cut for lysis. Cells or lung tissues were blended with cool PBS and Ripa lysis solution added with protease inhibitor, respectively. Protein loading buffer was added to protein solution and heat at 95 °C for 5 minutes. After electrophoresis and membrane transfer, the protein containing PVDF film were incubated with 5% BSA for 1 h. After TBST washing, PVDF film were incubated with 1:1000 primary antibodies at 4 °C overnight. Unbound antibodies were washed with TBST three times. Next, 1:10000 secondary antibodies were added to cells and incubated at 37 °C for 1 h. Unbound antibodies were washed with TBST three times. Chemiluminescence imaging was applied for protein band visualization.

Histological and immunofluorescence staining

Hematoxylin and eosin (H&E) staining, Sirius red staining and Masson's trichrome staining were conducted by Wuhan Servicebio Technology Co., Ltd, and the images were taken on tissue paraffin WS-10 scanner with NDP view 2 (Zhiyue Medical Technology, Hefei) and quantified by Image J 1.53 u. All statistical analysis was performed on 3-4 different areas in 5-6 biologically independent specimens following manufacturer's protocols (Abcam). Frozen or paraffin sections of lung tissues and cells growing on the glass slide were applied for immunofluorescence staining. The primary and secondary fluorescent antibodies and the corresponding dilution factors are listed in Table S7. Immunofluorescence images were scanned by Vectra Polaris with Phenochart 1.0.8 software (Akoya, USA). Quantification was performed using using Image J 1.53 u with the same method as described above.

Animal models

All animal research was in compliance with ethical regulations approved by Peking University's Institutional Animal Care and Use Committee. The living environment of animals were maintained at ~ 25 °C and 40% humidity with a 12 h light/dark cycle, with free access to standard food and water unless otherwise stated. Animals were euthanized if they experienced rapid body weight loss of 15-20% of their original weight to ensure humane treatment. For models of bronchopulmonary dysplasia (BPD), 20 days pregnant female SD rat were intraperitoneally injected with LPS (0.25 mg/kg). Postpartum rats and newborn rats were placed in the box with 80% oxygen concentration for 21 days, both male and female pups were included to reflect the neonatal onset of BPD. For model of acute lung injury, 8-week-old male C57BL/6J mice were intratracheally administrated LPS of 50 μL (2.5 mg/kg). For pulmonary fibrosis model, 8-week-old male C57BL/6J mice were intratracheally administrated bleomycin sulfate of 50 μL (2 U/kg). Male animals were selected for the acute lung injury and pulmonary fibrosis experiments based on established protocols and clinical relevance as supported by previous literature²⁵. All wild-type healthy mice used in this study were 8-week-old male C57BL/6J. Wild-type healthy newborn Sprague-Dawley (SD) rats included both sexes.

In vivo expression and inflammation detection for PL LNPs

mLuc PL LNPs were intratracheally administrated to healthy mice or rat. At 6 h after administration, bioluminescence imaging was performed to evaluate lung Luc protein expression using IVIS imaging

system (Perkin Elmer). At 24 h, mice were anesthetized by intraperitoneal injection of chloral hydrate. A longitudinal incision on the neck was cut using surgical scissors, and the trachea is exposed by separating muscles. The trachea was cut open with a small hole and the retention needle is inserted into the trachea about one centimeter. Then, 800 μL of PBS was infused into the lung twice to collect bronchoalveolar lavage (BAL). The obtained BAL was centrifuged at 500 g for 3 min and the supernatant were collected for ELISA assay according to manufacturer's protocol.

In vivo expression and inflammation detection for NAIP LNPs

mLuc NAIP LNPs were intratracheally administrated to healthy mice (0.2 mg/kg). At 2 and 6 h after administration, bioluminescence imaging was performed using IVIS imaging system (Perkin Elmer). Then, mice were euthanized and blood and lungs were collected. 50 mg of lung was lysed with 1x Promega Luciferase Assay System Cell Culture Lysis Reagent. For luciferase expression, 5 μL of lysed supernatant and 50 μL of luciferin solution were loaded onto a white 96 well-plate, and the bioluminescence was measured by BioTek synergy H1 microplate reader. 50 mg of lung was lysed with trizol and extracted mRNA for qPCR assay. The remaining lung tissue was digested and decomposed into single-cell suspensions for detecting immune cell infiltration in lung by flow cytometry. Blood was centrifuged at 8000 g for 3 min and collected serum for measuring IL-6 levels by ELISA assay.

In vivo expression and inflammation for UA containing ALC-0315 and cKK-E12 LNPs

mLuc LNPs with ALC-0315 and cKK-E12 formulations adding with/without UA were intratracheally administrated to healthy mice (0.2 mg/kg). At 6 and 24 h after administration, bioluminescence imaging was performed using IVIS imaging system (Perkin Elmer). Then, mice were euthanized and BAL, blood and lungs were collected. 50 mg of lung was lysed with trizol and extracted mRNA for qPCR assay. Blood was centrifuged at 8000 g for 3 min and collected serum for measuring IL-6 levels by ELISA assay. The obtained BAL was centrifuged at 500 g for 3 min and the supernatant were collected for ELISA assay according to manufacturer's protocol.

In vivo expression for BPD rats and IPF mice

BPD rat model with high oxygen treatment for 14 days was established as previously described. mLuc LNPs were intratracheally administrated to BPD rats (0.2 mg/kg). At 6 h after administration, bioluminescence imaging was performed to evaluate lung Luc protein expression using IVIS imaging system (Perkin Elmer).

IPF mice model was established as previously described. mLuc LNPs were intratracheally administrated to IPF mice (0.2 mg/kg). At 6 h after administration, bioluminescence imaging was performed to evaluate lung Luc protein expression using IVIS imaging system (Perkin Elmer).

mRNA delivery and expression in the LoxP-EGFP mice

To evaluate mRNA expression on different cells in the lung, mCre LNPs (0.8 mg/kg) were intratracheally administrated to LoxP-flanked EGFP reporter mice. After 48 h treatment, cell isolation and staining were performed, then analyzed by flow cytometry. For lung tissue perfusion, the left atrium was perforated and lungs were perfused through the right ventricle with 5 ml of dPBS until completely white. 2500 U Collagenase I, 30 U Neutral Protease and 500 U Deoxyribonuclease (DNase) I were used for lung digestion. Dissected lungs were digested in 5 ml of enzyme mixture by gentleMACS™ Octo Dissociator with the procedure of lung_01_02 three times, 37 °C_m_LIDK_1 once and lung_01_02 three times. The cell suspension was filtered through 40 μm filter and resuspended in cold 1×RBC lysis buffer and dPBS. Cell types were distinguished by specific markers by flow cytometry (Epithelial cells: CD326⁺, Immune cells: CD326⁻ and CD45⁺, Endothelial

cells: CD326⁻, CD45⁻ and CD31⁺, Stroma cells: CD326⁻, CD45⁻ and CD31⁻. The percentage of EGFP⁺ cells in each cell populations were measured and quantified.

Efficacy study

BPD rat models (21 days) were established as previously described. At day 3, 8, 13 and 18, the rats were treated with PBS, PL32 LNPs containing mFGF10, P-UA LNPs containing mFGF10 and mNR1D1 at a concentration of 0.6 mg/kg and empty PL32 LNP and P-UA LNP with the same lipid concentration by tracheal administration. Rat weight was recorded every two days. At day 24, the rats were sacrificed, and blood, BAL and lung tissue were collected for white blood cell detection, ELISA assay, tissue slicing, ROS and SOD measurement.

IPF models in C57BL/6J mice were developed as previously described. At day 3, 8, 13 and 18 after administration of bleomycin, the mice were treated with PBS, PL32 and P-UA LNPs containing mNR1D1 with a concentration of 0.6 mg/kg and empty PL32 LNP and P-UA LNP with the same lipid concentration by tracheal administration. On the third day after the last administration, the mice were executed and BLA and lung tissues were collected. IL-1 β , IL-6 and TNF- α concentration in BAL were measured by ELISA assay. Lung tissues were used for detecting immune cells by flow cytometry and slicing stain.

Lyophilization of LNPs

mLuc containing P-UA LNPs were prepared by microfluidics and dialyzed in phosphate sucrose buffer overnight. Dialyzed LNP were diluted to 0.04 mg/mL of mLuc by adding phosphate sucrose buffer. In the case of freeze-drying, type I glass vials (7 ml) were filled with 1 mL of the diluted mLuc LNP containing 40 μ g of mLuc. Freeze drying is carried out as previously described in Figure S19c.

Inhaled delivery of LNPs in vivo

mLuc containing LNPs for nebulization inhalation were prepared as previously described. LNPs were atomized by Aeroneb vibrating mesh nebulizer and atomized LNP droplets were collected. The mLuc concentration was measured by Quant-it RiboGreen RNA assay. mLuc containing LNPs were intratracheally administrated to healthy mice. At 6 h after administration, mice were euthanized and lungs were removed. The bioluminescence imaging was performed to evaluate lung Luc protein expression using IVIS imaging system (Perkin Elmer).

To study the inhaled delivery of PL32 and P-UA LNPs in large animals, male beagle dogs (~8 kg, Marshall BioResources) were acclimatized for at least 14 days before experiments. Beagle dogs were anaesthetized with isoflurane in oxygen using a nose-only exposure mask. AerogenSolo nebulizer was connected to the nose-only exposure mask and mLuc containing PL32 and P-UA LNPs were nebulized and inhaled by the dogs at a dose of 0.3 mg/kg. At 12 h after administration, dogs were executed and bioluminescence images and luciferase expression detection were taken following the same process as described above. Moreover, the blood, BAL and lung tissues were collected for routine blood test, ELISA assay and HE stain.

Freeze-dried mNR1D1 P-UA LNPs were reconstituted by adding nuclease-free water. Three BPD rats or IPF mice were placed in the atomization inhalation device. 0.04 mg/mL mNR1D1 P-UA LNPs were added to AerogenSolo nebulizer and administered dose of atomization is 8 mg/kg per mouse/rat of mNR1D1. Therapeutic schedules were the same as the previously described.

Statistics

Data are expressed as the mean \pm SEM as indicated in each of the figure legend. Statistical significance was determined using a two-tailed unpaired Student's *t*-test when only two value sets were compared or by ANOVA for comparison between multiple groups via Prism 9.5. Exact *P* values are documented in the figures or figure legends.

Difference was considered to be significant if *P* < 0.05, (**P* < 0.05, ***P* < 0.01, ****P* < 0.001, *****P* < 0.0001 unless otherwise indicated).

Reporting summary

Further information on research design is available in the Nature Portfolio Reporting Summary linked to this article.

Data availability

All data supporting the findings of this study are presented in the main article, supplementary information, and source data file. All data have been deposited in the Figshare database under accession code (<https://figshare.com/s/d089cf6aae9acc332264>). The datasets generated by genome-wide CRISPR Screening in this study have been deposited in the NCBI database under accession code PRJNA1276887. The datasets generated by bulk RNA-Seq in this study have been deposited in the NCBI database under accession code PRJNA1277717. The datasets generated by proteomics in this study have been deposited in the ProteomeXchange/iProX repository under accession code PXD065130. Any remaining information can be obtained from the corresponding author upon reasonable request. Source data are provided with this paper.

References

- Wang, C., Zhang, Y. B. & Dong, Y. Z. Lipid Nanoparticle-mRNA Formulations for Therapeutic Applications. *Acc. Chem. Res.* **54**, 4283–4293 (2021).
- Melamed, J. R. et al. Ionizable lipid nanoparticles deliver mRNA to pancreatic β cells via macrophage-mediated gene transfer. *Sci. Adv.* **9**, eade1444 (2023).
- Liu, S. et al. Membrane-destabilizing ionizable phospholipids for organ-selective mRNA delivery and CRISPR-Cas gene editing. *Nat. Mater.* **20**, 701 (2021).
- Miao, L. et al. Delivery of mRNA vaccines with heterocyclic lipids increases anti-tumor efficacy by STING-mediated immune cell activation. *Nat. Biotechnol.* **37**, 1174 (2019).
- Zhang, L. Z. et al. Effect of mRNA-LNP components of two globally-marketed COVID-19 vaccines on efficacy and stability. *Npj Vaccines* **8**, 156 (2023).
- Cheng, Q. et al. Selective organ targeting (SORT) nanoparticles for tissue-specific mRNA delivery and CRISPR-Cas gene editing. *Nat. Nanotechnol.* **15**, 313 (2020).
- Shan, X. Z. et al. RNA nanotherapeutics with fibrosis overexpression and retention for MASH treatment. *Nat. Commun.* **15**, 7263 (2024).
- Magadum, A., Kaur, K. & Zangi, L. mRNA-Based Protein Replacement Therapy for the Heart. *Mol. Ther.* **27**, 785–793 (2019).
- Rohner, E., Yang, R., Foo, K. S., Goedel, A. & Chien, K. R. Unlocking the promise of mRNA therapeutics. *Nat. Biotechnol.* **40**, 1586–1600 (2022).
- Israeli, E. IL-1 and IL-1ra are key regulators of the inflammatory response to RNA vaccines. *Isr. Med Assoc. J.* **24**, 257–257 (2022).
- Tahineni, S. et al. IL-1 and IL-1ra are key regulators of the inflammatory response to RNA vaccines. *Nat. Immunol.* **23**, 532 (2022).
- Yang, K. et al. Biodegradable Lipid-Modified Poly(Guanidine Thioctic Acid)s: A Fortifier of Lipid Nanoparticles to Promote the Efficacy and Safety of mRNA Cancer Vaccines. *J. Am. Chem. Soc.* **146**, 11679–11693 (2024).
- Gao, M. Z. et al. Modulating Plaque Inflammation Targeted mRNA Nanoparticles for the Treatment of Atherosclerosis. *ACS Nano* **17**, 17721–17739 (2023).
- Bai, X. et al. Inhaled siRNA nanoparticles targeting inhibit lung fibrosis and improve pulmonary function post-bleomycin challenge. *Sci Adv* **8**, eabn7162 (2022).
- Zhao, Z. Q. et al. Emerging nanotherapeutics for antithrombotic treatment. *Biomaterials* **255**, 120200 (2020).

16. Ndeupen, S. et al. The mRNA-LNP platform's lipid nanoparticle component used in preclinical vaccine studies is highly inflammatory. *Iscience* **24**, 103479 (2021).
17. Patel, M. N. et al. Safer non-viral DNA delivery using lipid nanoparticles loaded with endogenous anti-inflammatory lipids. *Nat Biotechnol* (2025).
18. Bitounis, D., Jacquinet, E., Rogers, M. A. & Amiji, M. M. Strategies to reduce the risks of mRNA drug and vaccine toxicity. *Nat. Rev. Drug Discov.* **23**, 281–300 (2024).
19. Xu, Y. D. et al. Delivery of mRNA Vaccine with 1, 2-Diesters-Derived Lipids Elicits Fast Liver Clearance for Safe and Effective Cancer Immunotherapy. *Adv Healthc Mater* **13**, e2302691 (2024).
20. Miao, L., Zhang, Y. & Huang, L. mRNA vaccine for cancer immunotherapy. *Mol Cancer* **20**, 41 (2021).
21. Omo-Lamai, S. et al. Lipid Nanoparticle-Associated Inflammation is Triggered by Sensing of Endosomal Damage: Engineering Endosomal Escape Without Side Effects. *bioRxiv* (2024).
22. Zhang, H. W. et al. Rational design of anti-inflammatory lipid nanoparticles for mRNA delivery. *J. Biomed. Mater. Res A* **110**, 1101–1108 (2022).
23. Davies, N. et al. Functionalized lipid nanoparticles for subcutaneous administration of mRNA to achieve systemic exposures of a therapeutic protein. *Mol. Ther. Nucl. Acids* **24**, 369–384 (2021).
24. Wang, C. R., Zhao, C. Y., Wang, W. P., Liu, X. Q. & Deng, H. Z. Biomimetic noncationic lipid nanoparticles for mRNA delivery. *P Natl Acad. Sci. USA* **120**, e2311276120 (2023).
25. Cheng, M. et al. Development of Organ Targeting Lipid Nanoparticles with Low Immunogenicity and Its Application in the Treatment of Pulmonary Fibrosis. *Angewandte Chemie International Edition* (2024).
26. Wang, S. Y. et al. Accelerating diabetic wound healing by ROS-scavenging lipid nanoparticle-mRNA formulation. *P Natl Acad. Sci. USA* **121**, e2322935121 (2024).
27. Rubey, K. M. & Brenner, J. S. Nanomedicine to fight infectious disease. *Adv Drug Deliver Rev* **179**, 113996 (2021).
28. Su, K. X. et al. Reformulating lipid nanoparticles for organ-targeted mRNA accumulation and translation. *Nat Commun* **15**, 5659 (2024).
29. Li, B. W. et al. Combinatorial design of nanoparticles for pulmonary mRNA delivery and genome editing. *Nat. Biotechnol.* **41**, 1410 (2023).
30. Shan, X. et al. RNA nanotherapeutics with fibrosis overexpression and retention for MASH treatment. *Nature Communications* **15** (2024).
31. Lokugamage, M. P. et al. Optimization of lipid nanoparticles for the delivery of nebulized therapeutic mRNA to the lungs. *Nat. Biomed. Eng.* **5**, 1059–1068 (2021).
32. Couture-Sénéchal, J., Tilstra, G. & Khan, O. F. Engineering ionizable lipids for rapid biodegradation balances mRNA vaccine efficacy and tolerability. *bioRxiv* (2024).
33. Sun, M. Z. et al. Targeted Therapy of Osteoarthritis via Intra-Articular Delivery of Lipid-Nanoparticle-Encapsulated Recombinant Human FGF18 mRNA. *Adv Healthc Mater* **13**, e2400804 (2024).
34. Zhang, K. L., Mishra, A. & Jagannath, C. New insight into arginine and tryptophan metabolism in macrophage activation during tuberculosis. *Front Immunol* **15**, 1363938 (2024).
35. Pérez, S. & Rius-Pérez, S. Macrophage Polarization and Reprogramming in Acute Inflammation: A Redox Perspective. *Antioxid.-Basel* **11**, 1394 (2022).
36. Gouda, N. A., Alshammari, S. O., Abourehab, M. A. S., Alshammari, Q. A. & Elkamhawy, A. Therapeutic potential of natural products in inflammation: underlying molecular mechanisms, clinical outcomes, technological advances, and future perspectives. *Inflammopharmacology* **31**, 2857–2883 (2023).
37. Su, J. B., Yu, M. H., Wang, H. C. & Wei, Y. L. Natural anti-inflammatory products for osteoarthritis: From molecular mechanism to drug delivery systems and clinical trials. *Phytother. Res* **37**, 4321–4352 (2023).
38. Wang, B. B. et al. Integrative analysis of pooled CRISPR genetic screens using MAGeCKFlute. *Nat. Protoc.* **14**, 756–780 (2019).
39. Mounkes, L. C., Zhong, W., Cipres-Palacin, G., Heath, T. D. & Debs, R. J. Proteoglycans mediate cationic Liposome-DNA complex-based gene delivery and. *J. Biol. Chem.* **273**, 26164–26170 (1998).
40. VasanthaKumar, T. & Rubinstein, J. L. Structure and Roles of V-type ATPases. *Trends Biochem Sci.* **45**, 295–307 (2020).
41. Wang, F. J., Gómez-Sintes, R. & Boya, P. Lysosomal membrane permeabilization and cell death. *Traffic* **19**, 918–931 (2018).
42. Skowyra, M. L., Schlesinger, P. H., Naismith, T. V. & Hanson, P. I. Triggered recruitment of ESCRT machinery promotes endolysosomal repair. *Science* **360**, 49 (2018).
43. Kirkegaard, T. et al. Hsp70 stabilizes lysosomes and reverts Niemann-Pick disease-associated lysosomal pathology. *Nature* **463**, 549–U171 (2010).
44. Enzer, K. G., Baker, C. D. & Wisniewski, B. L. Bronchopulmonary Dysplasia. *Clin. Chest Med* **45**, 639–650 (2024).
45. Miller, A. N., Shepherd, E. G., El-Ferzli, G. & Nelin, L. D. Multidisciplinary bronchopulmonary dysplasia care. *Expert Rev. Resp. Med* **17**, 989–1002 (2023).
46. Thébaud, B. et al. Bronchopulmonary dysplasia. *Nat. Rev. Dis. Prim.* **5**, 174–180 (2019).
47. Bolte, C. et al. Nanoparticle Delivery of Proangiogenic Transcription Factors into the Neonatal Circulation Inhibits Alveolar Simplification Caused by Hyperoxia. *Am. J. Resp. Crit. Care* **202**, 100–111 (2020).
48. Chen, Y. R. et al. Pollen-Inspired Shell-Core Aerosol Particles Capable of Brownian Motion for Pulmonary Vascularization. *Adv. Mater.* **35**, e2207744 (2023).
49. Giusto, K., Wanczyk, H., Jensen, T. & Finck, C. Hyperoxia-induced bronchopulmonary dysplasia: better models for better therapies. *Dis Model Mech* **14**, dmm047753 (2021).
50. Hurskainen, M. et al. Single cell transcriptomic analysis of murine lung development on hyperoxia-induced damage. *Nature Communications* **12**, 1565 (2021).
51. O'Reilly, M. & Thébaud, B. Animal models of bronchopulmonary dysplasia. The term rat models. *Am. J. Physiol.-Lung C* **307**, L948–L958 (2014).
52. Wang, S., Li, F., Lin, Y. K. & Wu, B. J. Targeting REV-ERB α for therapeutic purposes: promises and challenges. *Theranostics* **10**, 4168–4182 (2020).
53. Wang, Q. X. et al. Circadian clock molecule REV-ERB α regulates lung fibrotic progression through collagen stabilization. *Nat Commun* **14**, 1295 (2023).
54. Wu, J., Chu, X., Chen, C. & Bellusci, S. Role of Fibroblast Growth Factor 10 in Mesenchymal Cell Differentiation During Lung Development and Disease. *Front Genet* **9**, 545 (2018).
55. Yuan, T., Volckaert, T., Chanda, D., Thannickal, V. J. & De Langhe, S. P. Fgf10 Signaling in Lung Development, Homeostasis, Disease, and Repair After Injury. *Front Genet* **9** (2018).
56. Sundar, I. K., Rashid, K., Sellix, M. T. & Rahman, I. The nuclear receptor and clock gene REV-ERB α regulates cigarette smoke-induced lung inflammation. *Biochem Biophys Res Co.* **493**, 1390–1395 (2017).
57. Liu, T. J., Rinke, A., Flaherty, K. & Phan, S. H. Potential role of myeloid-derived suppressor cells in pulmonary fibrosis. *J Immunol* **202**, 182.3 (2019).
58. van Geffen, C. et al. Regulatory Immune Cells in Idiopathic Pulmonary Fibrosis: Friends or Foes? *Front Immunol* **12**, 663203 (2021).
59. Mi, S. et al. Blocking IL-17A Promotes the Resolution of Pulmonary Inflammation and Fibrosis Via TGF- β 1-Dependent and -Independent Mechanisms. *J. Immunol.* **187**, 3003–3014 (2011).

60. Nie, Y. J., Wu, S. H., Xuan, Y. H. & Yan, G. Role of IL-17 family cytokines in the progression of IPF from inflammation to fibrosis. *Military Med Res* **9**, 21 (2022).
61. Banerjee, S. & Kane, P. M. Regulation of V-ATPase Activity and Organelle pH by Phosphatidylinositol Phosphate Lipids. *Front Cell Dev Biol* **8**, 510 (2020).
62. Hurley, J. H. & Hanson, P. I. Membrane budding and scission by the ESCRT machinery: it's all in the neck. *Nat. Rev. Mol. Cell Bio* **11**, 556–566 (2010).
63. Schoonenberg, V. A. C. et al. CRISPRO: identification of functional protein coding sequences based on genome editing dense mutagenesis. *Genome Biol* **19**, 169 (2018).
64. Chen, C. H. et al. Improved design and analysis of CRISPR knockout screens. *Bioinformatics* **34**, 4095–4101 (2018).
65. Sanson, K. R. et al. Optimized libraries for CRISPR-Cas9 genetic screens with multiple modalities. *Nat Commun* **9**, 5416 (2018).
66. Xu, H. et al. Sequence determinants of improved CRISPR sgRNA design. *Genome Res* **25**, 1147–1157 (2015).
67. Ma, T. et al. Low-dose metformin targets the lysosomal AMPK pathway through PEN2. *Nature* **603**, 159 (2022).

Acknowledgements

This research was financially supported by National Key Research and Development Program of China (2023YFC3405000 to L.M.), Beijing Natural Science Foundation (Z220022, to L.M.), Beijing Municipal Science & Technology Commission (Z231100007223012 to L.M.), the National Natural Science Foundation of China (NSFC) grants (HY2021-8, 82373807 to L. M. Peking University People's Hospital Scientific Research Development Funds (RDJ2022-10 to J.D.), Clinical Medicine Plus X-Young Scholars Project, Peking University, the Fundamental Research Funds for the Central Universities (PKU2024LCXQ004 to J.D. and L.M.) the National Natural Science Foundation of China (NSFC grant 32030064 and 32250013 to Z.W.) the National Key Research and Development Program of China (MOST grant 2021YFA1300503 to Z.W.) and the National Natural Science Foundation of China (No. 22175188 to X.L.). We thank the State Key Laboratory of Natural and Biomimetic Drugs, Peking University Biological Imaging Facility for confocal, animal, and tissue imaging services.

Author contributions

L.M., Z.Q.Z., X.Z.S. and J.D. are responsible for all phases of the research. Z.Q.Z., X.Z.S., J.D., B.M., Y.A.F., J.H.C., C.L.S., C.L.W., S.R.Z. and Y.X.L. performed experiments. B.Y.L., Q.Q.Y. and W.D.H. conducted the CRISPR screening experiments and analysis. S.L. and X.D.C. helped with the process-optimization for lyophilization and atomization. Z.Q.Z., X.Z.S. and L.M. wrote the manuscript. H.K.W., C.L., S.K.S., X.Q., Z.F.W.,

X.G.L. and L.M. provided conceptual advice and supervised the study. All the authors discussed the results and assisted in the preparation of the manuscript.

Competing interests

L.M., Z.Q.Z. and X.Z.S. have filed a patent for the development of the described NIF LNPs. The remaining authors declare no competing interests.

Additional information

Supplementary information The online version contains supplementary material available at <https://doi.org/10.1038/s41467-025-61688-z>.

Correspondence and requests for materials should be addressed to Jing Ding, Zefeng Wang, Xueguang Lu or Lei Miao.

Peer review information *Nature Communications* thanks Fangfang Cao and the other, anonymous, reviewer(s) for their contribution to the peer review of this work. A peer review file is available.

Reprints and permissions information is available at <http://www.nature.com/reprints>

Publisher's note Springer Nature remains neutral with regard to jurisdictional claims in published maps and institutional affiliations.

Open Access This article is licensed under a Creative Commons Attribution-NonCommercial-NoDerivatives 4.0 International License, which permits any non-commercial use, sharing, distribution and reproduction in any medium or format, as long as you give appropriate credit to the original author(s) and the source, provide a link to the Creative Commons licence, and indicate if you modified the licensed material. You do not have permission under this licence to share adapted material derived from this article or parts of it. The images or other third party material in this article are included in the article's Creative Commons licence, unless indicated otherwise in a credit line to the material. If material is not included in the article's Creative Commons licence and your intended use is not permitted by statutory regulation or exceeds the permitted use, you will need to obtain permission directly from the copyright holder. To view a copy of this licence, visit <http://creativecommons.org/licenses/by-nc-nd/4.0/>.

© The Author(s) 2025

¹State Key Laboratory of Natural and Biomimetic Drugs, School of Pharmaceutical Sciences, Peking University, Beijing, China. ²Beijing Key Laboratory of Molecular Pharmaceutics, School of Pharmaceutical Sciences, Peking University, Beijing, China. ³Department of Pharmaceutics, Wuya College of Innovation, Shenyang Pharmaceutical University, Shenyang, China. ⁴Department of Pediatrics, Peking University People's Hospital, Beijing, PR China. ⁵Shanghai Institute for Nutrition and Health, Chinese Academy of Sciences, Shanghai, China. ⁶Peking University International Cancer Institute, Beijing, China. ⁷State Key Laboratory of Molecular Oncology, Peking University Cancer Hospital & Institute, Beijing, China. ⁸Beijing Key Laboratory of Carcinogenesis and Translational Research, Department of Lymphoma, Peking University Cancer Hospital & Institute, Beijing, China. ⁹Peking University-Yunnan Baiyao International Medical Research Center, Beijing, China. ¹⁰University of North Carolina at Chapel Hill, North Carolina, USA. ¹¹Beijing National Laboratory for Molecular Sciences, CAS Key Laboratory of Colloid, Interface and Chemical Thermodynamics, Institute of Chemistry, Chinese Academy of Sciences, Beijing, China. ¹²University of Chinese Academy of Sciences, Beijing, China. ¹³Department of Hepatobiliary and Pancreatic Surgery, the First Affiliated Hospital of Zhejiang University School of Medicine, Hangzhou, Zhejiang, China. ¹⁴School of Life Science, Southern University of Science and Technology, Shenzhen, China. ¹⁵These authors contributed equally: Zhiqiang Zhao, Xinzhu Shan, Jing Ding, Bin Ma. ✉e-mail: dingjingvv@126.com; wangzf@sustech.edu.cn; xueguang@iccas.ac.cn; lmiao_pharm@bjmu.edu.cn